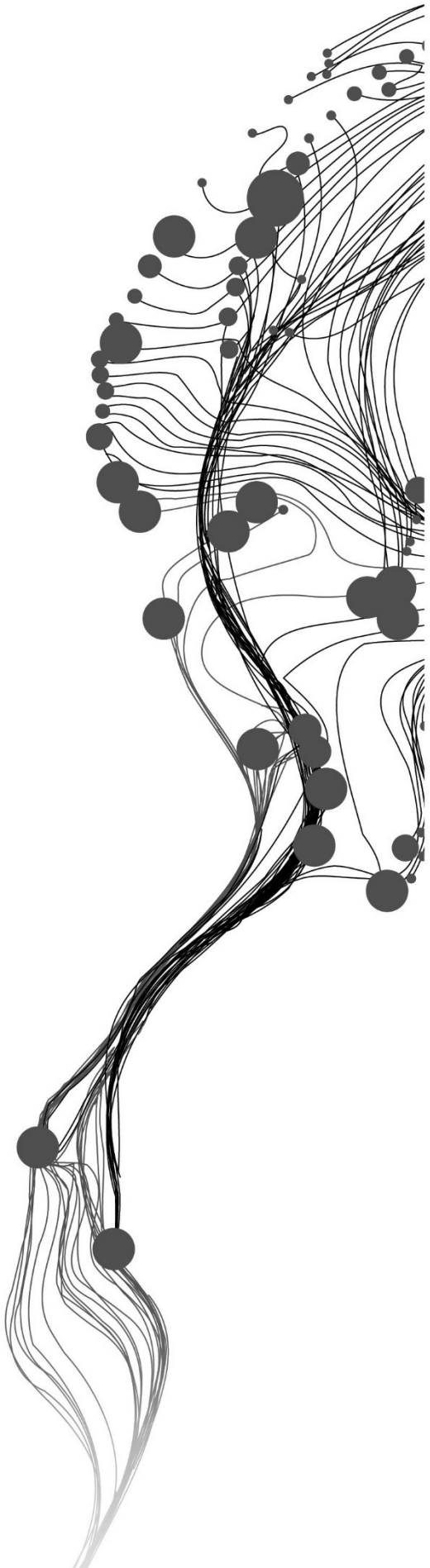


**Monitoring and characterisation of
opencast mining induced land
deformation by using PolSAR and
DInSAR techniques**

SURAJIT KAR
MARCH, 2017

SUPERVISORS:
Mr Vinay Kumar
Dr Valentyn Tolpekin
Dr R S Chatterjee



Monitoring and characterisation of opencast mining induced land deformation by using PolSAR and DInSAR techniques

[SURAJIT KAR]

Enschede, The Netherlands, [MARCH, 2017]

Thesis submitted to the Faculty of Geo-Information Science and Earth Observation of the University of Twente in partial fulfilment of the requirements for the degree of Master of Science in Geo-information Science and Earth Observation.

Specialisation: Geoinformatics

SUPERVISORS:

Mr Vinay Kumar

Dr Valentyn Tolpekin

Dr R S Chatterjee

THESIS ASSESSMENT BOARD:

Chair: Prof. Dr Ir Alfred Stein.

External Examiner: Dr Sanjay.

ITC Supervisor: Dr Valentyn Tolpekin.

ITC Observer: Drs. J P G Bakx.

IIRS Supervisor: Mr Vinay Kumar.

IIRS Advisor: Dr R S Chatterjee.

IIRS Observer: Dr Sameer Saran.

DISCLAIMER

This document describes work undertaken as part of a programme of study at the Faculty of Geo-Information Science and Earth Observation of the University of Twente. All views and opinions expressed therein remain the sole responsibility of the author, and do not necessarily represent those of the Faculty.

ABSTRACT

Opencast mining is a dynamic field in terms of surface profile changes. Surface profile changes occur due to the continuous extraction of minerals and over burdens. Land deformation is very common phenomena in and around opencast mine area. Spaceborne synthetic aperture radar is a commanding tool to monitor opencast mine induced land deformation, including identification of mining indicators. In this literature, various polarimetric decomposition methods such as H/A/ α and Yamaguchi four-component decomposition has been studied to identify various mining indicators and their properties. Various Differential Interferometric SAR (DInSAR) techniques applicable to time series single polarised SAR data to extract land deformation information has been discussed. A fusion technique is implied to integrate land deformation information and opencast mining properties have been studied. Jharia coalfield in India is considered as a study area. In this study, fully polarimetric SAR data are used to identify mining indicators and their properties; and time series single polarised SAR data are used to find out land deformation information by Permanent Scatterer Interferometric Synthetic Aperture Radar (PSInSAR) technique. The effect of polarisation orientation angle shift on opencast mine topography has been generated. Integrated land deformation information and opencast mining indicators and their properties have been generated from Discrete Wavelet Transform (DWT). A high rate of land deformation (landslide, land subsidence and land uplift) was observed in and around opencast mine area. The effect of land deformation due to opencast mining activities was lesser as one goes away from the opencast mine. Heavy Earth Moving Machinery (HEMM), opencast active mine faces, opencast mine floor mixed with soil and rocks with/without water, benches and terraces of opencast mines and mass wasting phenomena represent opencast mining indicators and their properties.

Keywords: SAR, DInSAR, PSInSAR, PolSAR, PolSAR decomposition methods, H/A/ α decomposition, Yamaguchi four-component decomposition, Image fusion, Discrete wavelet transform, opencast mining.

ACKNOWLEDGEMENTS

First and foremost my sincerest gratitude goes towards my father, mother, masima, brother, sister, dada and Sara for providing me with their continued support in my academic achievements so far.

I want to express my hearty thankfulness to all my teachers from IIRS and ITC for helping me with their vast knowledge and also for technically supporting me throughout this course.

I would like to express my deepest sense of obligation and gratefulness to my supervisor Mr Vinay Kumar, from IIRS for being my source of continuous encouragement. He has provided constant support and motivation towards completing this research work.

Dr Valentyn Tolpekin, my supervisor from ITC, who is unique as a guide and also as a teacher. I highly admire his technical knowledge, constant support, positive criticism and most importantly providing guidance and time when needed the most. His promptness and clarity in emails helped me to shape my research work properly. Dear Sir, thank you for helping me throughout and it has been a privilege for me to work under your guidance, which I will cherish all throughout my life. I am grateful to you.

Dr R S Chatterjee, my advisor as well as a mentor from IIRS is a person with clarity in thoughts and ideas. His in-depth knowledge and constant guidance were a boon for me. He has been a strong guiding force all throughout my research work. I have been honoured and feel blessed to have a supervisor like him. Thank you, sir, for providing new ideas and helping all throughout.

I also like to thank Dr S. K. Srivastav, Group Head, Remote Sensing and Geoinformatics group, for solving all our problems and guiding with necessary advice when required. Special thanks to Dr Valentyn Tolpekin and Dr Sameer Saran M.Sc. Course Directors for providing me with the necessary guidance and support during my M.Sc. Course work. My warm regards go to Dr A Senthil Kumar, Director, IIRS for his timely help and support in all possible ways.

My heartfelt appreciation and thanks go to my best friends Sayan Mukhopadhaya, Soham Mukherjee, Arijit Panda, Vaibhav Raj, Daman deep Singh, Reshma Jeswani, Indranil Nandi, Jyoti Prakash Hati, Sutapa Bhattacharjee, Sk. Ariful Hossain. They are my source of smile and confidence. I would also thank all my M.Sc. batch mates (2014-16 and 2016-18), M.Tech. batch mates (2014-16, 2015-17 and 2016-18) and PG diploma batch mates (2014-16, 2015-17 and 2016-18) friends. Their constant support, encouragement, help and among all their most valuable friendship will be cherished. I would also thank all my M.Sc. batch mate friends at ITC.

Special appreciation goes to the CMA team and all IIRS staffs for providing me with their continuous technical and nontechnical support during my research work.

Thank you, everyone, who was important towards completing this research work of my M.Sc. dissertation and I express my sincere apologies for not being able to mention all the names individually.

Surajit Kar.

TABLE OF CONTENTS

LIST OF FIGURES.....	iv
LIST OF TABLES.....	vi
1. INTRODUCTION.....	7
1.1. Background.....	7
1.2. Motivation and problem statement.....	7
1.3. Research objectives.....	11
1.4. Research questions.....	11
1.5. Innovation aimed at.....	12
1.6. Thesis structure.....	12
2. OVERVIEW OF POLSAR AND POLSAR DECOMPOSITION METHODS.....	13
2.1. PolSAR.....	13
3. LITERATURE REVIEW.....	18
3.1. Polarisation orientation angle (θ) shift in PolSAR data.....	18
3.2. Identification of HEMM.....	18
3.3. InSAR.....	19
3.4. DInSAR.....	20
3.5. ADInSAR.....	21
3.6. Opencast mining induced land deformation monitoring using PSInSAR.....	22
3.7. Data fusion.....	22
4. STUDY AREA, DATA SET AND TOOLS USED.....	24
4.1. Study area.....	24
4.2. Data set used.....	25
4.3. Tools used.....	26
4.4. Data for Validation.....	26
5. RESEARCH METHODOLOGY.....	27
5.1. Research workflow.....	28
5.2. Polarisation orientation angle shift in PolSAR data.....	29
5.3. PolSAR data processing for identification of various opencast mining indicators.....	29
5.4. Mining properties identification.....	30
5.5. PSInSAR processing.....	32
5.6. Integrated information obtained from PolSAR and PSInSAR data analysis and visualisation.....	32
6. RESULTS.....	33
6.1. Estimation of Polarisation orientation angle shift (θ).....	33
6.2. Polarimetric responses of mining properties.....	34
6.3. Identification of HEMM.....	37
6.4. Identification of active mining faces.....	39
6.5. Identification of opencast mining properties.....	40
6.6. Land deformation information from PSInSAR technique.....	42
6.7. Integrated information obtain from PolSAR and ADInSAR technique.....	45
7. DISCUSSION, CONCLUSION AND RECOMMENDATIONS.....	47
7.1. Discussion.....	47
7.2. Conclusion.....	48
7.3. Answer to the research questions.....	49
7.4. Recommendation.....	50
LIST OF REFERENCES.....	51

LIST OF FIGURES

Figure 1: Opencast Mine	7
Figure 2: Heavy Earth Moving Machinery (HEMM) in Opencast mine	7
Figure 3: Various scatterings mechanism	16
Figure 4: Study area Jharia coal field from SAR (Pauli RGB image, R: HH-VV; G: HV; B: HH-VV) images	24
Figure 5: Red pixel represents HEMM and green pixel represent other than HEMM of ground truth data in LISS IV image of Jharia coal field	26
Figure 6: Flowchart	28
Figure 7: Location of four opencast mines within study area	30
Figure 8: Polarisation orientation angle shift estimation of 2011 scene (left image), zoom mining area (right image) and histogram of polarisation orientation angle shift estimation (below image)	33
Figure 9: Polarisation orientation angle shift estimation of 2010 scene (left image), zoom mining area (right image) and histogram of polarisation orientation angle shift estimation (below image)	34
Figure 10: Yamaguchi Polarimetric responses of various mining properties	36
Figure 11: Entropy and Anisotropy responses of various mining properties	36
Figure 12: Green point represents classified HEMM shown in LISS IV image of study area	37
Figure 13: Red point represents ground truth and green point represents classified points of HEMM shown in the LISS-IV image	37
Figure 14: Green points represents classified HEMM overlay on LISS-IV image	38
Figure 15: A - B HEMM classified image shown in Google earth image dated 30th October 2011	39
Figure 16: Identification of active opencast mine faces from HEMM location	39
Figure 17: Classified image of opencast mining properties	40
Figure 18: Opencast floor mixture with of soil and rock with no accumulated stagnant water	40
Figure 19: Opencast mine floor filled with water	41
Figure 20: Benches and terraces identified in classified image	41
Figure 21: Classification image of mass wasting phenomena	42
Figure 22: Normal baseline distance in Y axis and temporal extent in X axis of 20 numbers of time series ENVISAT data	42
Figure 23: Land deformation information in Google Earth image	43
Figure 24: Land deformation information in Jharia coalfields	43
Figure 25A-D: Rate of land deformation observed at particular point over time series	44
Figure 26: Fusion technique of mining properties obtained from PolSAR technique and time series land deformation information obtained from PSInSAR technique	45

[Figure 27: Fusion image of land deformation information and mining properties](#)45

LIST OF TABLES

- [Table 1: Specification of Polarimetric SAR data used](#)25
- [Table 2: Specification of single polarised SAR data used](#).....25
- [Table 3: Summary of ground truth data](#).....26
- [Table 4: Effect of polarisation orientation angle shift on the elements of coherency matrix](#).....34
- [Table 5: Mining indicators and their polarimetric responses](#)35

1. INTRODUCTION

1.1. Background

Minerals such as coal and petroleum are the main sources of energy needed in modern human civilisation. Minerals are found to be deposited inside the Earth's crust. Two major mining techniques are used to extract minerals such as underground mining technique and opencast mining technique. The underground mining technique is used predominantly for deeper extraction of minerals. However, opencast mining (as shown in Figure 1) comes into consideration when minerals are found in shallow depth. In the present mining scenario of India, the extraction of total amount of coal is higher from opencast mines than underground mines (Ghose, 2007). Similarly, even globally the extraction of total amount of minerals is higher from opencast mines than underground mines (Hustrulid and Clark, 2016). Also, larger hazards are taking place due to opencast mining activities compared to underground mine activities. Opencast mining activities affect the surrounding environment. Environment related hazards are land deformation, air pollution from contamination of dust from mine, and change in terrain characteristic due to land deformation from mining activity. Recently, it is also observed that there is a paradigm shift in mining scenario from underground mining to opencast mining both in India and globally.

Nowadays, opencast mines are getting into deeper layers of Earth's crust to extract minerals profitably and efficiently. As a result, bench height to bench width ratio is observed to increase during extraction of minerals. Thus, the overall slope angle of opencast mines is observed to increase, making opencast mining projects more profitable. Therefore, benches of the opencast mines are unable to sustain and this could result in slope failure (Jayanthu and Reddy, 2008). Besides, safety in opencast mine decreases with time due to a higher ratio of bench height to bench width. As a result, land deformation is common phenomena in and around the opencast deep mining areas (Hustrulid and Clark, 2016; Jayanthu and Reddy, 2008). Moreover, land deformation is also induced by underground mine activities.



Figure 1: Opencast Mine
(Geomartin, 2009).



Figure 2: Heavy Earth Moving Machinery (HEMM) in Opencast mine
(Heavy Equipment, 2016).

1.2. Motivation and problem statement

In the case of underground mines, minerals are extracted from below the earth surface without removing the overburden by using bord and pillar method and longwall method (Hartman and Mutmanský, 2002). Therefore, underground mining operation creates a void below the Earth surface. Roof strata carry its own

load. Additional supports are provided to carry the load of the roof strata. When support is inadequate, sag is formed in the roof strata bedding plane. The sag in roof strata results in bed separation of the rock strata. Consequently, fractures and dome of disturb zones are formed in the rock strata (Bell et al., 2000). Land deformation induced by underground mining is a vertical displacement of land. Land subsidence results in the formation of cracks on the surface, which eventually forms a cavity within the ground (Altun et al., 2010). As a result, the roof rock collapses during mining or after a long period (Ng et al., 2009). The consequence of land subsidence is roof fall in an underground mine and creation of pothole on the surface.

On the contrary, in opencast mining scenario, excavation of land for extraction of mineral and dumping of overburden rocks in the rim area can result in terrain instability. This is more pronounced in the case of weak and fragile rocks like fractured shale and sandstone. Besides, groundwater extraction to facilitate opencast mining operations (Loupasakis et al., 2014) and a resulting reduction in the pore water pressure of the underlying aquifer causes compaction of the aquifer and overlying rock layers (Erban et al., 2014). As a result, land subsidence occurs within the mining area and opencast rim area (Erban et al., 2014). This may lead to the development of wide cracks in the mining area (bench and terrace), opencast mine slope and rim area, and finally, causing mass wasting phenomena such as a landslide or debris flow.

In the case of land deformation, the strength of rock strata gradually decreases depending upon the increase of cumulative stress in the rock strata (Wang, 1981). The following are the opencast mining indicators and their properties those are responsible for increase in stresses in the rock strata cause land deformation in opencast mining areas:

- Active mining faces where removal of overburden (OB) and extraction of the mineral is going on are important. Heavy Earth Moving Machinery (HEMM) (as shown in Figure 2) are deployed in large mechanised opencast mines that increase the rate of extraction of minerals and removal of overburden (Dhillon and Anude, 1992; Jayanthu and Reddy, 2008). A movement of active faces or benches is observed when the position of faces changes over time due to extraction. The movement of active faces is observed when mineral or overburden extraction is going on (Kulshreshtha and Parikh, 2002).
- Geometric characteristics of the bench and terrace (entrance of opencast mine) are also responsible for land deformation. Geometric characteristics of the bench include bench height, bench width, the slope angle of the bench, and the overall slope of open pit mine (Osasan and Afeni, 2010).
- Slope properties also accelerate the land deformation. Slope properties are various types of slope such as steep or gentle. The overall slope of opencast mine changes due to the extraction of mineral and overburden. There is a high probability of land deformation when the overall slope of opencast mine become steeper (Osasan and Afeni, 2010).
- The topographical characteristic of opencast quarry rim area (the area around the opencast mine up to which area the impact of land deformation can be related) is also important. Land use land cover (LULC) and presence or absence of fracture are also important factors for land deformation in an opencast quarry fringe area.
- Mass wasting phenomenon (mass movement) is the downward movement of opencast mine benches due to gravity. Mass wasting phenomena may result in a landslide and land subsidence. Land deformation due to mass movement is very common if loose rock masses are present in a steep slope (Savage, 1951).

Land deformation depends on the spatial extent and intensity of opencast mining. The properties of opencast mining indicators and the rate of extraction of mineral and overburden can be used to infer on

potential land subsidence due to opencast mining. An adequate amount of manpower and costly equipment are deployed in opencast active mining faces. The consequences of land deformation and rock mass movement could be slope instabilities or slope failure (landslide) in an opencast mine (Paradella et al., 2015). The landslide and land subsidence in an active mine faces result in loss of lives, loss of costly equipment, loss of production and productivity, loss of working days and working environment, and loss of labour safety (Pankow et al., 2014). A slope failure results in mass wasting phenomena such as landslide and debris flow, land subsidence, and land collapse. Also, some other consequences of land deformation are observed around the opencast fringe area.

The land deformation implies a change in terrain over time observed around the opencast quarry fringe (rim) area. As opencast mining is a continuous process with variable depth in order to extract minerals, there are some spatial pattern and position can exist in the deformation. Thus, it will be interesting to assess the deformation patterns and determine how it affects the change in terrain over time. Land deformation causes displacement and may result in the collapse of the ground, surface infrastructures like roads, bridges, buildings, and as well as other linear (pipeline, electricity cable) and point features are affected (Raspini et al., 2016). Land deformation also disturbs the nearby river courses and other surface water features (Loupasakis et al., 2014). Also, change in land use land cover is observed in the opencast quarry fringe (rim) area due to land deformation. So, monitoring of opencast induced land deformation is necessary.

Various techniques, methods, and equipment are used for identification and monitoring of opencast mine induced land deformation. Previously ground-based monitoring equipment and the geotechnical instruments were very common to monitor land deformation in opencast mines (Jarosz and Wanke, 2004). Ground-based conventional surveying instruments are referred as ground-based monitoring equipment in the previous line were used to measure positional changes. The geotechnical instruments are crack measuring pins, inclinometers, extensometers, tilt-meters, piezometers and micro-seismic geophones (Jarosz and Wanke, 2004). The positional accuracy of GPS-based land deformation monitoring system depends on the distribution of satellites position present during received signals over a large opencast mine's slope angle geometric constraints (Yang et al., 2012). Though numerous equipment are used to monitor opencast mine land deformation still, land deformation is one of the major problems of opencast mine (Jakóbczyk et al., 2015). The limitation of this type of equipment includes limited spatial coverage of the mine, complex data management and high cost (Jarosz and Wanke, 2004). Ground movement measurement techniques can be divided into two categories such as discrete points surface measurements by using instruments such as the total station, and extensometer; and surface measurement by area based scanning techniques using ground-based radar, laser and an image based remote sensing techniques (Paradella et al., 2015). Area based scanning techniques of surface measurement provide information about the spatial pattern of land deformation (Paradella et al., 2015). Image based remote sensing techniques have some advantages over terrestrial techniques.

All the terrestrial equipment (described in the previous paragraph) including laser scanning slope monitoring and Ground Based Synthetic Aperture Radar (GBSAR) are required to install or operate for each face or part of the face. In contrast, remote sensing has the advantage of the main spatial movement patterns measurement without field work over the total station, reflecting prisms or ground-based synthetic aperture radar techniques (Pinto et al., 2015). Also, ground based land deformation measurement equipment requires more time to monitor and has limited spatial extent. On the other hand, the satellite-based approach is more convenient to cover the whole opencast mine and image analysis technique is widely used for identification, classification and monitoring of various properties.

Though, various spectrum regions such as optical, infrared, and microwave are used for spaceborne image analysis, microwave based image analysis has the capability of cloud penetration which increases detail information in image and all time (day and night) operational capabilities over the optical and infrared spectra

(Rosen et al., 2000). Therefore, spaceborne Synthetic Aperture Radar (SAR) generated image analysis technique is efficient to monitor land deformation and can able to identify the opencast mining indicators and their properties (illustrated earlier) to reveal land deformation phenomena in the opencast mining area.

The common practice of land deformation and slope stability monitoring is to monitor each of the mining faces or parts of mining faces. But the extension of the land deformation is also observed around the opencast mine rim area which also affects land use and land cover change. The surface profile of opencast mine has been generated by using Interferometric Synthetic Aperture Radar (InSAR) technique (Paradella et al., 2015; Mura et al., 2014). The interferogram is generated by using two SAR images of the same area from two different acquisition position of the satellite (Crosetto, 2002). Differential Interferometric Synthetic Aperture Radar (DInSAR) technique provides an arithmetic difference of phase between two InSAR images. Nowadays, DInSAR technique has become more popular to monitor land deformation (Hu et al., 2014). Different SAR techniques have centimetre to sub-centimetre precision to detect land displacement over a long period of time and in a large areal extent (Colombo and Tre, 2013) although, spaceborne SAR has some constraints.

SAR image has inherent geometric distortion problem due to side-looking geometry. Also, the geometric constraint of opencast mine includes geometric distortion especially in deep opencast mine region where opencast mine has varying slope angle. Geometric distortions happen due to foreshortening, layover, and shadow (Lee and Pottier, 2009; Esmailzade et al., 2015). Due to geometric distortion, interferogram generation may fail in case of opencast mine.

Interferogram generation may fail partially due to geometric distortion in SAR images of opencast mine. Information obtained from both ascending and descending SAR image pairs can be a solution for interferogram generation failure due to geometric distortion (Crosetto, 2002). The low coherence in an interferogram image pair leads to unsuccessful interferogram generation (Ferretti et al., 2007). The main cause of low coherence is surface profile changes in SAR images taken at various acquisition time (Sousa et al., 2010). Surface profile changes observed due to the mining operation, landslide and land subsidence, heavy rainfall, and positional changes of HEMM. Phase error in SAR signal is responsible for positional changes of the earth surface incorporated by the atmosphere. Spatial de-correlation occurs between SAR image pair due to large baseline. Interferogram generation failure due to phase unwrapping problem can be overcome by using adequate quality of Digital Elevation Model (DEM). Known topography provided as a DEM can be used to correct interferogram (Ferretti et al., 2007). But the surface profile of opencast mine changes over time. So, the surface profile obtained from InSAR technique may be a solution for the adequate quality DEM. If interferogram generation failure occurs, reasons for failure are to be explored during research work. Advanced DInSAR (A-DInSAR) techniques such as Persistent Scatterers Interferometry (PSI) also overcome the unsuccessful interferogram generation limitation of DInSAR technique (Pinto et al., 2015). A-DInSAR technique has been used to monitor land deformation in opencast mine (Paradella et al., 2015; Mura et al., 2016).

Identification of opencast mining properties can be done by using PolSAR data. Characteristic of benches, traces and slope properties such as steep or gentle slope can be identified by receiving polarised wave after interaction with the opencast surface properties. Opencast surface properties include geometrical structure, shape, reflectivity, orientation, surface roughness. Receiving polarised wave has a different polarisation due to the interaction with different target than the incident electromagnetic wave and store the information in scattering matrix. Coherence and covariance matrix are generated from scattering matrix (Verma, 2012). The polarisation orientation angle shift is very common phenomena in PolSAR scene. The angle between the major axis of the polarisation ellipse and the horizontal axis is called polarisation orientation angle. The effective pixel area is affected by polarisation orientation angle shift and misinterpretation of different surface properties happen due to the orientation angle shift (Verma, 2012). So, problem is to be expected

for identification of characteristic of benches, terrace and slope properties of opencast mine by using polarimetric decomposition properties. Compensation of the effect of orientation angle shift can be a solution to the problem by estimating orientation angles from the PolSAR data or by using DEM obtained from InSAR process (Lee et al., 2000).

Identification and monitoring of mining properties that relate to land deformation are very important to reduce land deformation in opencast mines. Therefore, from the above discussion, it can be concluded that spaceborne A-DInSAR monitoring system is justified for land deformation monitoring in an opencast mine. However, DInSAR techniques cannot be used to detect the opencast mining properties that indicate land deformation. On the other hand, PolSAR data provides better information about the identification of various properties (Lakshmi et al., 2012). So, opencast mining properties can be identified from PolSAR data. Therefore, identification of opencast mining indicators and their properties can be done by using PolSAR techniques; and which can further be integrated with time series of DInSAR land deformation to explore the spatial relation between opencast mining and land deformation including the nature and intensity of deformation. Suitable pixel based data fusion technique is to be explored to integrate information obtained from PolSAR data and land deformation from time series analysis of DInSAR data. Also, the effect of orientation angle shift in the PolSAR image is to be explored during the research work.

Though researches have been carried out on identification, monitoring and characterisation of underground mining induced land subsidence by using DInSAR technique, limited work has been carried out on monitoring and characterisation of opencast mining induced land deformation (Paradella et al., 2015). Moreover, integration of Polarimetric Synthetic Aperture Radar (PolSAR) and Differential Interferometric Synthetic Aperture Radar (DInSAR) based information will enable us to identify land subsidence related to opencast mining and associated impacts. To identify opencast mining induced land deformation, it is required to extract opencast mining related properties and to relate them with land deformation in and around opencast quarries. These properties are active mining faces, geometric characteristic of the benches and terraces, slope properties, and affected quarry rim area which may be retrieved by PolSAR decomposition and analysis of scattering properties. Long term land deformation history can be obtained by time series DInSAR data analysis.

1.3. Research objectives

To explore PolSAR for identification of opencast mining indicators and their properties, and their spatial relation with time series PSInSAR deformation to characterise opencast mining induced land deformation.

These are sub-objectives through which the main objective can be achieved.

- 1) To identify opencast mining indicators and their properties based on decomposition properties from PolSAR data.
- 2) To monitor opencast mining induced land deformation by time series analysis of PSInSAR based data processing.
- 3) To explore the relationship between land deformation and opencast mining indicators and their properties to characterise opencast mining induced land deformation.

1.4. Research questions

- 1) What is the influence of polarisation orientation angle on PolSAR data of opencast mine topography?
- 2) Which of the polarimetric signatures and decomposition methods are best suited for identification of mining indicators and their properties responsible for opencast mine induced land deformation?
- 3) What are the spatial patterns and position of land deformation identified by time series analysis of

PSInSAR process?

- 4) Is DInSAR fail in specific mine area? In which state DInSAR process failed and which respective characteristic or property of opencast mine is responsible for the failure?
- 5) How to integrate the PolSAR and PSInSAR results?

1.5. Innovation aimed at

Information obtained from PolSAR for identification of opencast mining indicators and their properties, and to integrate them with time series PSInSAR land deformation to explore the spatial relation between opencast mining properties and land deformation including the nature and intensity of deformation.

1.6. Thesis structure

This research work is organised into following chapters. The first chapter covers a brief introduction to this research, objectives to be accomplished and research formulated based on the objectives. The Second chapter refers to the overview of PolSAR and PolSAR decomposition methods. The third chapter describes the literature review of previous work that has been done related to this research work and the methods used. The fourth chapter is about the study area and the dataset used. The fifth chapter explains about the methodology and the methods adopted. The experimental results and discussion summaries are included in the sixth chapter. Finally, the conclusions of the research with recommendations for future work are presented in the chapter seventh.

2. OVERVIEW OF POLSAR AND POLSAR DECOMPOSITION METHODS

2.1. PolSAR

PolSAR is polarimetric synthetic aperture radar. The locus of the polarised wave represents the polarisation of an electromagnetic wave. Amplitude is determined by the length of the electric field vector, and frequency is denoted by a number of rotation cycles of the wave per unit time. The orientation and shape of pattern trace by the tip of the vector represent the polarisation such as horizontal polarisation, vertical polarisation, circular polarisation, elliptical polarisation. The electric field vector of an electromagnetic wave can be polarised or unpolarised (random) or a combination of both (NRC, 2014).

Horizontally or vertically polarimetric wave is transmitted and horizontally or vertically polarimetric wave is received in the case of PolSAR data. Fully polarised or polarimetric electromagnetic wave has the following four combinations of polarisation such as:

HH – The horizontally polarised wave is transmitted and the horizontally polarised wave is received.

HV – The horizontally polarised wave is transmitted and the vertically polarised wave is received.

VH – The vertically polarised wave is transmitted and the horizontally polarised wave is received.

VV – The vertically polarised wave is transmitted and the vertically polarised wave is received.

The HH and VV are called co-polarized or like polarised and the HV and VH are called cross polarised (NRC, 2014).

When polarised wave interacts with target or scatterer the polarisation of the electromagnetic wave is changed and information store in scattering matrix as follows (Lee and Pottier, 2009).

$$[S] = \begin{bmatrix} S_{HH} & S_{HV} \\ S_{VH} & S_{VV} \end{bmatrix}. \quad (2.1)$$

S_{HH} is the element of scattering matrix where the horizontal electromagnetic wave is transmitted and horizontal electromagnetic wave is received.

S_{HV} is the element of scattering matrix where the horizontal electromagnetic wave is transmitted and vertical electromagnetic wave is received.

S_{VH} is the element of scattering matrix where the vertical electromagnetic wave is transmitted and horizontal electromagnetic wave is received.

S_{VV} is the element of scattering matrix where the vertical electromagnetic wave is transmitted and vertical electromagnetic wave is received.

S_{HH} and S_{VV} are the co-pol elements of scattering matrix, and S_{HV} and S_{VH} are the cross-pol elements of scattering matrix.

Fully polarimetric Synthetic Aperture Radar (PolSAR) data is to be used for identification (Lakshmi et al., 2012) of mining properties responsible for land deformation by identifying suitable polarimetric properties. Natural Resource Canada (2014) define polarimetric properties as mentioned below:

- (i) Total power: Total power = $|S_{HH}|^2 + |S_{HV}|^2 + |S_{VH}|^2 + |S_{VV}|^2$ and can be expressed as coherence and covariance matrices.

- (ii) Co-pol correlation coefficient: Co-pol correlation coefficient is expressed as $R = \frac{(S_{HH} S_{VV}^*)}{\sqrt{(|S_{HH}|^2 |S_{VV}|^2)}}$.
Where, superscript * represent the conjugate of the matrix.
- (iii) Co-pol phase difference: Co-pol phase difference is the average phase angle difference between the corresponding pixels or group of the pixel. It is characteristic of a number of bounces. Identification of roughness or smoothness can be done with this parametric property.
- (iv) Degree of polarisation: Degree of polarisation is the ratio of the power in the polarised part to the total power in an electromagnetic wave. Expressed as $D_{pol} = \frac{\sqrt{(S_1^2 + S_2^2 + S_3^2)}}{S_0}$. The Stoke's parameter S_0 is the total power in a wave while $\sqrt{(S_1^2 + S_2^2 + S_3^2)}$ is total power in the polarisation part.
- (v) Coefficient of variation: Coefficient of variation is the ratio of the difference of maximum power (P_{max}) and minimum power (P_{min}) to the maximum power. Expressed as $\frac{P_{max} - P_{min}}{P_{max}}$. P is the power in a polarisation signature.

In the case of the polarimetric radar system, the total scattered power is represented by span. Such as $Span = Tr(S S^{*T}) = |S_{HH}|^2 + |S_{HV}|^2 + |S_{VH}|^2 + |S_{VV}|^2 = |S_{HH}|^2 + 2|S_{HV}|^2 + |S_{VV}|^2$ by considering $|S_{HV}|^2 = |S_{VH}|^2$. Where $Tr()$ represents trace of a matrix; superscript * and T represent conjugate and transpose of a matrix, respectively (Lee and Pottier, 2009).

Two major approaches are present for classification of PolSAR images. The approaches are lexicographic covariance matrix approach based on physically measurable parameters and another is coherency matrix approach based on orthogonal Pauli matrix components (Gao and Ban, 2008). Coherency and covariance matrix will be generated from scattering matrix and both matrices can be linearly transformed into one another as follows.

$$\langle T \rangle = N \langle C \rangle N^T \quad (2.2)$$

Where, T is coherency matrix; C is covariance matrix; and

$$N = \frac{1}{\sqrt{2}} \begin{bmatrix} 1 & 0 & 1 \\ 1 & 0 & -1 \\ 0 & \sqrt{2} & 0 \end{bmatrix} \quad (2.3)$$

and superscript T denotes transpose of a matrix and $\langle \rangle$ indicates the ensemble average of data processing (Gao and Ban, 2008).

Pauli vector K_p is generated as follows (Singh et al., 2013).

$$K_p = \frac{1}{\sqrt{2}} \begin{bmatrix} S_{HH} + S_{VV} \\ S_{HH} - S_{VV} \\ 2S_{HV} \end{bmatrix} \quad (2.4)$$

Coherency matrix is to be generated from scattering matrix. Coherency matrix

$$\langle [T_3] \rangle = \langle K_p K_p^\dagger \rangle = \begin{bmatrix} T_{11} & T_{12} & T_{13} \\ T_{21} & T_{22} & T_{23} \\ T_{31} & T_{32} & T_{33} \end{bmatrix} \quad (2.5)$$

$$= \frac{1}{2} \begin{bmatrix} |S_{HH} + S_{VV}|^2 & (S_{HH} + S_{VV})(S_{HH} - S_{VV})^* & 2(S_{HH} + S_{VV})S_{HV}^* \\ (S_{HH} - S_{VV})(S_{HH} + S_{VV})^* & |S_{HH} - S_{VV}|^2 & 2(S_{HH} - S_{VV})S_{HV}^* \\ 2S_{HV}(S_{HH} + S_{VV})^* & 2S_{VH}(S_{HH} - S_{VV})^* & 4|S_{HV}|^2 \end{bmatrix} \quad (2.6)$$

Where, † represents complex conjugation and the transpose of a matrix and $\langle \rangle$ indicates the ensemble average of data processing (Kajimoto and Susaki, 2013). Various PolSAR decomposition methods are applied on coherency matrix or covariance matrix for identification and classification of scatterers.

2.1.1. PolSAR decomposition methods

Only second-order polarimetric representations such as a 3×3 Hermitian matrix generated from covariance and coherency matrices can be used to analyse distributed scatterers. Due to the presence of the speckle noise, distributed scatterers can only be characterised statistically (Lee and Pottier, 2009).

Applying reflection symmetry condition in the covariance matrix, 3 components decomposition of the PolSAR image has been done by Freeman and Durden, (1998). The reflection symmetry condition is $\langle S_{HH}S_{HV}^* \rangle = \langle S_{VV}S_{HV}^* \rangle = 0$. To decompose natural distributed targets, the Freeman and Durden 3 components decomposition is a powerful technique based on simple physical scattering mechanisms such as single bounce scattering, double bounce scattering and volume scattering (Freeman and Durden, 1998). Other various PolSAR decomposition methods are available for identification and classification of distributed scatterers such as

- (i) Yamaguchi 4 components decomposition (Yamaguchi et al., 2005).
- (ii) Singh 4 components decomposition (Singh et al., 2013).
- (iii) Entropy (H)/Anisotropy (A)/ Alpha (α) decomposition (Lee and Pottier, 2009).
- (iv) Multiple Component Scattering Model (MCSM) 5 components decomposition (Zhang et al, 2008).

H/A/ α decomposition developed by Cloude and Pottier. H/A/ α decomposition is considered the most frequently used method (Yamaguchi et al, 2010). The second most frequently used method is three components decomposition method developed by Freeman and Durden (Yamaguchi et al., 2010). Reflection symmetry does not hold for complicated geometric structures scattering in Freeman and Durden three components decomposition. So, in this research, Yamaguchi 4 components decomposition and H/A/ α decomposition has been used for identification of mining indicators and their properties.

(i) Yamaguchi 4 components decomposition.

Reflection symmetry does not observe i.e. $\langle S_{HH}S_{HV}^* \rangle \neq 0$ and $\langle S_{VV}S_{HV}^* \rangle \neq 0$ for complicated geometric structures scattering in an urban area. Reflection symmetry also vanishes for practically all natural distributed scattering. Helix scattering power component added to the single bounce scattering, double bounce scattering and volume scattering; and proposed 4 components decomposition by Yamaguchi et al. (2005) where, it was considered that reflection symmetry does not hold. The imaginary part of $T_{23} = \langle (S_{HH} - S_{VV}) S_{HV}^* \rangle$, the element of coherency matrix represents the helix scattering power (Singh et al., 2013). However, Lee and Ainsworth (2011) also concluded that the Freeman-Durden decomposition and the Yamaguchi decomposition do not utilize the full polarimetric information of the coherency matrix.

a. Single bounce scattering

First order Bragg surface scatterer such as rooftop gives surface or single bounce scattering. The phase difference is 0° in the case of single bounce scattering.

b. Double bounce scattering

Dihedral corner reflector such as ground and side of building together gives double bounce scattering models. The phase difference is $\pm 180^\circ$ in the case of double-bounce scattering.

c. Volume scattering

A set of randomly oriented dipoles generates volume scattering such as forest gives volume scatterings.

d. Helix scattering

Generally, complicated shapes of man-made structures produce helix scattering. Helix scattering mechanism disappears for almost all natural distributed scatterers but appears for the manmade features (Turkar and Rao, 2011). Helix scattering has also been observed due to the complex rock edges present in opencast mines area.

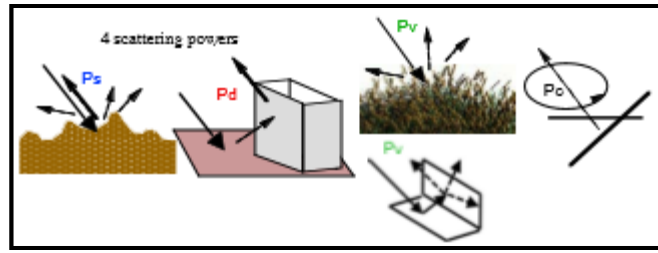


Figure 3: Various scatterings mechanism.

Figure 3 represents four components of scattering such as from left side surface scattering power (P_s), double bounce scattering power (P_d), volume scattering power (P_v), and helix scattering power (P_c) (Singh et al., 2013).

(ii) H/A/ α decomposition.

H/A/ α decomposition is also known as eigen decompositions of coherency matrix. The 3×3 Hermitian matrix can be decomposed as $\langle [T_3] \rangle = [U_3][\Sigma_3][U_3]^{-1}$ according to H/A/ α decomposition. Diagonal matrix $[\Sigma_3]$ contains the eigenvalues of $\langle [T_3] \rangle$; i.e.,

$$[\Sigma_3] = \begin{bmatrix} \lambda_1 & 0 & 0 \\ 0 & \lambda_2 & 0 \\ 0 & 0 & \lambda_3 \end{bmatrix} \quad (2.7)$$

Where, $\infty > \lambda_1 \geq \lambda_2 \geq \lambda_3 \geq 0$; and λ_i for $i=1, 2, 3$ represents the eigen value. The 3×3 unitary matrix $[U_3]$ contains the eigen vectors of $\langle [T_3] \rangle$; $[U_3] = [u_1 \ u_2 \ u_3]$ where $u_i = [\cos \alpha_i \ \sin \alpha_i \cos \beta_i e^{j\delta_i} \ \sin \alpha_i \cos \beta_i e^{j\delta_i}]$ for $i = 1, 2, 3$; each of u_1, u_2, u_3 is unit orthogonal eigenvector (Lee and Pottier, 2009). The primary parameters of eigen decomposition of $[T_3]$ are the eigenvalues and the eigenvectors. Three secondary parameters such as entropy (H); anisotropy (A); and mean alpha angle (α) are defined as a function of the eigenvalues and the eigenvectors of $[T_3]$ to generate physical information of scatterers (Lee and Pottier, 2009).

Entropy is defined as follows:

$$H = - \sum_{i=1}^3 P_i \log_3(P_i) \quad (2.8)$$

Where P_i is called the probability of the eigenvalue (λ_i); $P_i = \frac{\lambda_i}{\sum_{k=1}^3 \lambda_k}$.

The degree of randomness of the scattering process is denoted by the entropy (H). This is a measure of the domination of a given scattering mechanism within a resolution cell. $H \rightarrow 0$ means $\lambda_1 = \text{Span}$; $\lambda_2 = 0$; $\lambda_3 = 0$; so the rank of the coherence matrix $\langle [T_3] \rangle$ is 1 and it represents pure the target.

$H \rightarrow 1$ means $\lambda_1 = \frac{\text{Span}}{3}$; $\lambda_2 = \frac{\text{Span}}{3}$; $\lambda_3 = \frac{\text{Span}}{3}$; so the rank of the coherence matrix $\langle [T_3] \rangle$ is 3 and it represents distributed target.

$0 < H < 1$ means the final scattering results come from the combination of the three pure targets given by u_i for $i=1, 2, 3$ and weighted by the corresponding eigenvalue.

Anisotropy

$$A = \frac{\lambda_2 - \lambda_3}{\lambda_2 + \lambda_3} \quad (2.9)$$

Anisotropy represents the directional dependency of scatterers. This is quantifying how homogeneous a target is relative to radar look direction. Practically the anisotropy value can be used to discriminate the scatterers only when $H > 0.7$. Because, the second and third eigenvalues and also anisotropy are affected by the noise in case of lower entropy value, $H < 0.7$.

Mean α angle

$$\alpha = \sum_{i=1}^3 P_i \alpha_i \quad (2.10)$$

$\alpha \rightarrow 0$ means the scattering mechanism represents single bounce scattering from a surface.

$\alpha \rightarrow \frac{\pi}{2}$ means the scattering mechanism represents double bounce scattering.

$\alpha \rightarrow \frac{\pi}{4}$ means the scattering mechanism represents volume scattering.

Interpretation of scatterers is to be done on the basis of eigenvalues and eigenvectors provided by the Eigen decomposition of the coherency matrix. The $(1-H)(1-A)$, $H(1-A)$, and HA images represent the dominance of single bounce scattering, volume scattering and double bounce scattering, respectively (Lee and Pottier, 2009).

Identification of various mining properties can be done on the basis of their polarimetric responses such as single bounce, double-bounce, volume scattering, helix scattering, entropy, anisotropy. Various classifier such as minimum distance, maximum likelihood, parallelepiped can be applied on various target decomposition methods (Turkar and Rao, 2011) to classify various mining features. Maximum likelihood classifier provides better classification accuracy over minimum distance, Mahalanobis, parallelepiped classifier (Turkar and Rao, 2011).

3. LITERATURE REVIEW

This chapter describes the literature review of previous work and the methods used. Nowadays SAR or microwave remote sensing has become more popular for identification, classification and monitoring of the various target.

3.1. Polarisation orientation angle (θ) shift in PolSAR data

The off-diagonal terms of the coherency matrix or covariance matrix contain cross polarised returns. Many researchers set the off-diagonal terms to zero. According to Lee et al., (2001) such assumption is not valid especially for vegetated and rugged terrain areas. The information of the polarisation orientation angle induced by terrain azimuth slope is present in the real part of $\langle (S_{HH} - S_{VV}) S_{HV}^* \rangle$, the off-diagonal element of coherency matrix. The imaginary part of $\langle (S_{HH} - S_{VV}) S_{HV}^* \rangle$ gives information about helicity based on polarimetric decomposition theory of Krogager (Lee et al., 2001). The $\langle (S_{HH} - S_{VV}) S_{HV}^* \rangle$ term is also affected by the phase difference between S_{HH} and S_{VV} and the orientation angle shift. Also, the correlation between co and cross polarised returns is important here (Lee et al., 2001).

The polarisation orientation angle shifts induced by azimuthal slopes, occur as a result of the rotation about radar line of sight of the polarisation wave. The polarisation orientation angle can be defined by the following equation

$$\tan \theta = \frac{\tan \omega}{-\tan \gamma \cos \varphi + \sin \varphi} \quad (3.1)$$

Where, $\tan \omega$ is the slope in the azimuth direction, $\tan \gamma$ is the slope in the ground range direction, and φ is the radar look angle. The polarisation orientation angle shift is also affected by radar look angle and the range slope (Lee and Schuler, 2003). The azimuth slope can be either overestimated or underestimated when the range slope is positive (towards the radar) or negative (away from the radar) respectively (Lee and Schuler, 2003) due to the polarisation orientation angle shift induced by terrain slope (Lee et al., 2002) or rugged terrain area (Lee and Ainsworth, 2011). The range slope information is important for accurate estimation of azimuth slope (Lee and Schuler, 2003). The consequence of the orientation angle shift is the rotation of scattering matrix or coherency matrix around the radar line of sight (Lee et al., 2002) which results in the misinterpretation of scatterers. In general, the orientation angle shift due to the surface slope is lower if radar frequency is higher (Lee and Ainsworth, 2011). Lee and Ainsworth, (2011) found that after orientation angle compensation, the volume power is reduced and the double bounce power is magnified. The quantity of increase in double bounce power is higher than the quantity of decrease in volume power.

3.2. Identification of HEMM

It is a very challenging task to clearly distinguish between the target and target's background when almost similar responses are coming from the target and target's background. HEMM are very common in the opencast active mine faces for excavating the overburden and minerals. So, the identification of active mine faces can be done by identification of HEMM in an opencast mine. HEMM are the metallic objects with an approximate size of 10-20m \times 10-20m, which is more than the spatial resolution of an SAR image cell. Backscattering signal is stronger for the metallic object and appears as a bright spot compared to the background of SAR images (Ferdinando et al., 2012). Also, the HEMM is considered as a coherent structure. The largest eigenvalue with eigenvector is to be chosen to identify dominant scattering in a cell. In addition, the entropy value of the metallic object are low and the power of the scattered signal from the metallic object should be relatively high (Strzelczyk et al., 2014).

Several algorithms are present to identify metallic objects or coherent scatterers from SAR image. According to Strzelczyk et al., (2014), these algorithms are – (i) the coherent scatterers are distinguished by position in the range direction, position in the azimuth direction and height. So, the coherent structures can be detected in all the three spatial or spectral directions using a correlated object spectrum. Correlated object spectrum technique is established based on the correlation among two sub looks of the original image spectrum. However, if small bandwidth is considered for identification of coherent structure than a few strong coherent scatterers can be detected in this technique. So, the major disadvantage of this method strongly depends on the bandwidth (Schneider et al., 2006). (ii) The value of the signal to clutter ratio is also used to identify coherent scatterers. Clutter, the intensity of a calculated pixel is compared with the intensity of neighbouring pixels. A dB ratio higher than 15 is considered as coherent scatterers. Overestimation of clutter intensity is the major drawback of this method mainly observed in the highly dense urban area. (iii) If the value of amplitude dispersion (d_a) is small ($d_a < 0.25$) in the same pixel in multi-temporal images over time, then, that pixel is classified as coherent scatterers. However, a comparatively high number of SAR images are required to perform this method. (iv) Another method is based on the entropy (H) value obtained from fully polarimetric SAR data. The pixel has low entropy value ($H < 0.3$) classified as coherent scatterers where the system is considered as weakly polarised and pixels relate to point-like scatterers. However, the spatial averaging of the image using window kernel is performed in this method which reduces the spatial information. (v) Identification of polarised point scatterers can also be done using 2D filter considering eigenvalue or alpha threshold proposed by Cloude, (2009). (vi) On the basis of analysis of polarimetric signature, the identification of coherent scatterers in SAR images is done. This method gives accurate identification of coherent scatterers and also determines the scattering mechanism type from the analysis of scattering matrix. In the current research, low entropy value ($H < 0.3$) and high double bounce (> 0.01) are used to identify the HEMM opencast mines.

Identification of opencast active mining faces is done based on the location of HEMM identified in the opencast mine area.

3.3. InSAR

Synthetic aperture radar technique is an imaging technique operated in microwave spectra region. Interferometric Synthetic Aperture (InSAR) technique is a technique where single polarised electromagnetic waves are transmitted and received to acquire images. InSAR technique can be used for mapping or monitoring surface or target and also for surface profile generation. The interferogram is generated by using two SAR images of the same area taken from two different acquisition position of the satellite (Crosetto, 2002). Following is the general InSAR processing steps as described below.

First, pre-processing (co-registration, subset) is done by taking time series Single Look Complex (SLC) SAR data. An image corresponding to similar satellite passes i.e., either ascending (S-N) SAR or descending (N-S) image is selected. Co-registration is to be done by taking two images and considering one image as master and another as a slave. Master is the reference image and slave is another image which is to be aligned or co-registered with the master (Ferretti et al., 2007). The accuracy of co-registration should be less than the pixel size for obtaining better interferogram image. After pre-processing, the interferogram is generated by using the two images (viz., the master and the slave). SAR interferogram is generated by multiplying each complex number of the master image by the corresponding complex conjugate number of the slave image i.e. pixel by pixel cross multiplication. After interferogram generation, atmospheric correction, phase unwrapping, baseline correction, phase to height conversion, ortho-rectification are performed, and geocoded DEM is used to rectify the InSAR image. The time series of InSAR images can be obtained, when the time series of SAR images is considered as input in this InSAR procedure.

From two interferometric SAR image pair, the phase accuracy is estimated by the coherence. Coherence is the cross correlation coefficient of the two images. Coherence value ranges from zero (0) to one (1) where 1 means maximum coherence and 0 means no coherence. High coherence means less phase noise whereas less coherence means high phase noise. A movement of active faces or benches observes where mineral or overburden extraction is going on (Kulshreshtha and Parikh, 2002). Though, these changes are observed to be low and can be used to generate high coherence map. So, InSAR images are used to generate land deformation information in DInSAR process.

3.4. DInSAR

DInSAR generates an arithmetic phase difference between two InSAR profiles. According to Lu et al., (2013) the phase difference of interferogram images is expressed in the following equation

$$\Delta\psi_{\text{int}} = \Delta\psi_{\text{flat}} + \Delta\psi_{\text{topo}} + \Delta\psi_{\text{mov}} + \Delta\psi_{\text{atmos}} + \Delta\psi_{\text{noise}} \quad (3.2)$$

So, accuracy in phase is very important for accurate estimation of the phase difference. The precise orbit of the sensor and external Digital Elevation Model (DEM) are used for analytical calculation of the phase difference. Flat terrain and the topographic difference has influence in the phase difference of InSAR equation. Although, topographical components are removed in the phase difference of differential interferogram synthetic aperture radar images (Herrera et al., 2010). Phase noise mainly depends on temporal change, different look angles (existence of the critical baseline), volume scattering (Ferretti et al., 2007). DInSAR can also measure small surface deformation. Therefore, long-term land deformation history can be obtained from time series InSAR data analysis by using DInSAR process (Rosen et al., 2000).

Iron ore opencast mining induced land deformation was monitored using DInSAR by Mura et al. (2014) which delivered useful information about ground movement, mining risk assessment and planning. Opencast mine has a complex geometrical structure. Therefore, DInSAR is a challenging technique for monitoring and characterization of opencast mine induced land deformation (Paradella et al., 2015). DInSAR provides consistent and extensive information about non-linear ground deformation (Mura et al., 2016). In the singular non-urban environment especially in a mining area where

- (i) The presence of buildings, structures, and metallic objects are rare; and
- (ii) The rock outcrops and rock blocks are present; but
- (iii) Vegetation is absent;

the combination of above three factors has been proved to be appropriate for the detection of coherent pixels based approach (Herrera et al., 2010). SAR images corresponding to ascending and descending satellite passes are necessary to minimise the loss due to radar foreshortening, lay over, and shadow distortion and also to get vertical and horizontal components of land deformation (Paradella et al., 2015). C-band DInSAR is suitable to detect slow movement of subsidence areas whereas L-band DInSAR is suitable for identifying rapid movement subsidence areas (Chatterjee et al., 2015). Slow deformation can also be monitored using L-band DInSAR by increasing the temporal baseline between two InSAR acquisition images. All pixels of interferogram are not useful due to different decorrelation sources or phase degradation of pixels. Herrera et al., (2010) address two main techniques for pixel selection. These techniques are:

- (i) To find out the pixels corresponding to most stable backscattered radar signal (if its reflectivity in SAR images is constant) over time, in a set of SAR images, at full resolution. This technique is most suitable for man-made features or urban areas.
- (ii) To evaluate the coherence (the maximum likelihood estimator of the phase quality over an estimation window) and to find out the pixels whose pixel values are set over a given threshold

in the stack of interferogram images. This technique is most suitable for urban as well as non-urban reasons including the less vegetated areas.

A lot of studies were carried out on the identification, monitoring and characterisation of underground mining induced land subsidence by using DInSAR technique but limited work has been done on land deformation in opencast mines (Paradella et al., 2015). However, according to Mura et al., (2016) better accuracy is achieved by ADInSAR techniques, such as PSI than DInSAR time series.

3.5. ADInSAR

The adverse effect of the atmospheric influence on the propagating signal affecting accuracy and precision of the measurement of scatterers is overcome by using multiple SAR images in the advanced DInSAR techniques such as (i) Permanent (or Persistent) Scatterers (PS) InSAR technique for identification of stable backscattering objects over a long period of time. This technique is mainly used in urban area (Bitelli et al., 2015), (ii) Distributed Scatterers (DS) InSAR for identification of comparatively less stable backscattering areas which preserve coherence over a comparatively shorter time period than PS. This technique is mainly used in rural areas where permanent scattering objects are less (Bitelli et al., 2015), (iii) SqueeSAR technique for identification of scatterers is a combination of PSInSAR and DSInSAR methods (Bitelli et al., 2015).

However, Herrera et al., (2010) reported some limitations of the application of the A-DInSAR technique for detecting land deformations and landslides. These limitations are:

- (i) The displacement is calculated along the line of sight (LOS). The line of sight is the line defined by the ground target and the satellite sensor. The sensitivity of radar in detecting land displacement is more in parallel to the direction of the LOS than orthogonal to the LOS.
- (ii) The theoretical minimum detectable displacement between two consecutive SAR images is $\frac{\lambda}{4}$, where λ is the wavelength of radar's electromagnetic wave.
- (iii) The spatial resolution of land deformation's spatial pattern determines by the measurement point selection criteria.

PSInSAR has some added advantages than others.

3.5.1. PSInSAR

Persistent Scatterer Interferometry (PSI) is more suitable than the DInSAR time series for identifying most stable scattering pixels where pixel properties do not vary with time and radar look angle, in a stack of SAR images than DInSAR time series process (Mura et al., 2016). PSI allows individual point targets' temporal analysis of the interferometric phase. PSI technique provides better accuracy for the measurement of the surface target displacement than the DInSAR process. PSI also reduces the consequence of phase path delay which occurs during SAR image acquisition as a result of atmospheric heterogeneity. Phase unwrapping process in PSI technique is very important to accurately determine ground movement (Mura et al., 2016). Also, PSI has limited capability for the detection of high movement rate of displacement. However, PSI, combined with DInSAR time series process, allows the detection of high rate of linear and non-linear deformations (Mura et al., 2016).

The minimum displacement detection in PSI technique depends on the spatial density of the scatterers; the temporal resolution and the wavelength of SAR signal (Hartwig et al., 2013). To accomplish millimetre level precision of land displacement measurement in PSI technique, greater than 15 SAR pairs are required to generate a sufficient number of interferogram (Hartwig et al., 2013). Moreover, real-time monitoring is not possible in PSI technique.

3.6. Opencast mining induced land deformation monitoring using PSInSAR

Very few works have been carried out to monitor opencast mining induced land deformation using PSInSAR technique. Detection and monitoring of ground displacement were successfully done by using PSInSAR in the Oltrepo Pavese, Northern Italy which is considered as a complex geological and structural area (Meisina et al, 2006). PSI technique was also effectively applied in opencast mine area (Pinto et al., 2014). According to Pinto et al., (2015) PSI has the capability of providing high accuracy in case of long-term displacement monitoring in opencast mining areas, waste piles areas and opencast mine's surrounding region without any need of ground instruments and fieldwork. Monitoring of opencast iron mine has also been performed by using PSI technique (Paradella et al., 2015). Further, PSI technique has been used to monitor non-linear ground movement in opencast iron mine (Mura et al., 2016). Assessment of surface deformation in the post-mining area has been done by Milczarek et al., (2017) using PSI technique. According to Meisina et al., (2006) PS coherence (c) was classified into 3 classes such as $c < 0.65$; $0.65 \geq c \leq 0.85$; and $c > 0.85$. PS coherence value less than 0.65 should not consider because this will result in less reliability in the displacement measurement. Whereas, coherence value greater than 0.85 generates less number of PS points (Meisina et al., 2006). So, according to Meisina et al., (2006) PS coherence value should be selected between 0.65 to 0.85 for land deformation study. However, PSI technique has limitation to monitor rapid movement and 3D movement of any object. RTK (Rapid motion technique) can be used to monitor rapid movement and also for 3D movement (Iannacone and Falorni, 2016).

3.7. Data fusion

Number of satellites are increasing day by day and nowadays, various satellites also have multiple on-board sensors. Images acquired by numerous sensors have various specifications such as polarisation and various type of resolution viz., spatial, spectral, radiometric and temporal (Pohl et al., 1997). So, a wide range of significant details can be obtained from various images. Multiple relevant information come from two or more images require to combine the information in a single image by using multi-sensor image fusion or data fusion technique (Pohl et al., 1997). Such as higher spectral information of an area comes from one image and higher spatial information comes from another image of the same area, combine both the information and form a single image of higher spectral – higher spatial or increasing both the information in the output image (Pohl and Genderen, 2015). Nowadays, data fusion is an advanced and widely applied field. Data fusion technique is also popular for the performance of object recognition, sharpening the images, improve geometric corrections, enhance certain features, and replace the defective data (Dong et al., 2009). According to Dong et al., (2009) multi-sensor data fusion can be divided into four different fusion processing levels such as

- (i) Signal level data fusion: a better new signal (better signal to noise ratio) is created by combining input signals from various sensors.
- (ii) Pixel level data fusion: fusion operation is done at the pixel level. An improved image is generated from the sources images.
- (iii) Feature level data fusion: features are extracted from various source images and fusion is performed to form a single image at the feature level.
- (iv) Decision level data fusion: information are extracted from various source images and information fusion is performed at decision level.

According to Dong et al., (2009) some most popular, time efficient, effective, and at the same time relatively simple standard image fusion techniques are Principal Component Analysis (PCA), High Pass Filter (HPF), Intensity- Hue-Saturation (IHS), multi-resolution analysis based methods (e.g. pyramid algorithm, wavelet transformation), various arithmetic combination (e.g. Brovey transformation), and Artificial Neural Networks (ANNs).

However, some limitations of the above fusion techniques are as follows:

- (i) The co-registration of input images at sub-pixel level is important because pixel level fusion techniques are very sensitive to registration accuracy.
- (ii) The number of multiple spectral bands that can be taken as input should be ≤ 3 at a time for IHS and Brovey transformation.
- (iii) The standard image fusion techniques are some extent reduced the original spectral signature though successfully improve the spatial resolution.

According to Simone et al., (2002) the PCA and IHS fusion methods do not integrate the fine details of the scatterers in the output images whereas pyramidal methods are popular for preserving the fine details of the scatterers in the output images. The wavelet transform keeps the statistical parameters invariant and also reduces the colour distortion problem (Dong et al., 2009). The wavelet transformation is a commanding method which preserves the spectral characteristic of the multi-frequency and multi-polarised images (Simone et al., 2002).

3.7.1. Data fusion: Discrete Wavelet Transform (DWT)

Information obtained from single SAR data may be insufficient due to various slope angle and slope direction present in opencast mine. The information obtained from PolSAR data for identification of opencast mining indicators responsible for land deformation and land deformation information obtained from time series PSInSAR process of the same opencast mine may be combined by Discrete Wavelet Transform (DWT) (Simone et al., 2002; Hong et al, 2002; Simone et al, 2001). According to Simone et al., (2002) radiometric correction step is essential to decrease the effects of the significant changes of the reflection properties of the backscatters to normalise the pixel intensity, especially for the microwave and radio frequency sensors acquired images of the non-flat terrain. According to Ogden, (1997) in DWT method, an image is broken down into sub-images and computed by using high pass and low pass filters. The sub-images contain the frequency of the original image at the various level of resolution. After calculating the wavelet pyramid and combining the wavelet coefficients, the multi polarise and multi-frequency data is fused. According to Simone et al., (2002) each pyramid provides information considering the salience of each pattern which is denoted as the local energy of the incoming pattern within neighbourhood p i.e.

$$\hat{S}(i, j, k, l) = \sum_{i'j'} p(i'j') D(i + i', j + j', k, l)^2 \quad (3.3)$$

Where, \hat{S} is the salience measure,

p is the window function with unitary value where $1 \leq i' \leq r$ and $1 \leq j' \leq r$, and zero values elsewhere;

D is the pyramid structure of the image, and where (i, j, k, l) are the row sample position and column sample position, level and orientation indexes inside the pyramid structure.

The salient computation step is applied to each single pyramid of each image to be fused after measure the information combine capabilities from each pyramid. Finally, the inverse discrete wavelet transform is done to generate output fused image.

The output images of multi-polarization and multi-frequency fusion process are considered as input for the multiresolution fusion process and co-registration of images is done (Simone et al., 2002). Resampling operations are necessary when the difference between the spatial resolutions of two images is higher.

4. STUDY AREA, DATA SET AND TOOLS USED

This chapter deals with the study area of the research, satellite imageries of the study area and the tools used.

4.1. Study area

The Jharia Coal Field has a lot of significance in term of economic value in India. This coal field is located in the Dhanbad district of Jharkhand state in India. The Jharia Coal Field was selected as the study area for the proposed research work. Coal is extracted by both opencast as well as underground methods from this coal field. The Jharia Coal Field has 9 opencast mines and 23 underground mines (Gupta et al., 2014). Coking coal has advantages such as good carbon content and fewer impurities over non-coking coal. In India, coking coal is present only in Jharia coal field. Jharia coalfield has a long and diverse opencast as well as underground mining history over a century. Unplanned mining excavation in the past is also present in this study area. Unplanned mining operations result in mining induced land subsidence, the occurrence of fire, re-handling of overburden dumps, abandoned mining sites (Prakash and Gupta, 1998). Therefore, continuous change of land used pattern is observed thus triggering the requirement of monitoring this study area.

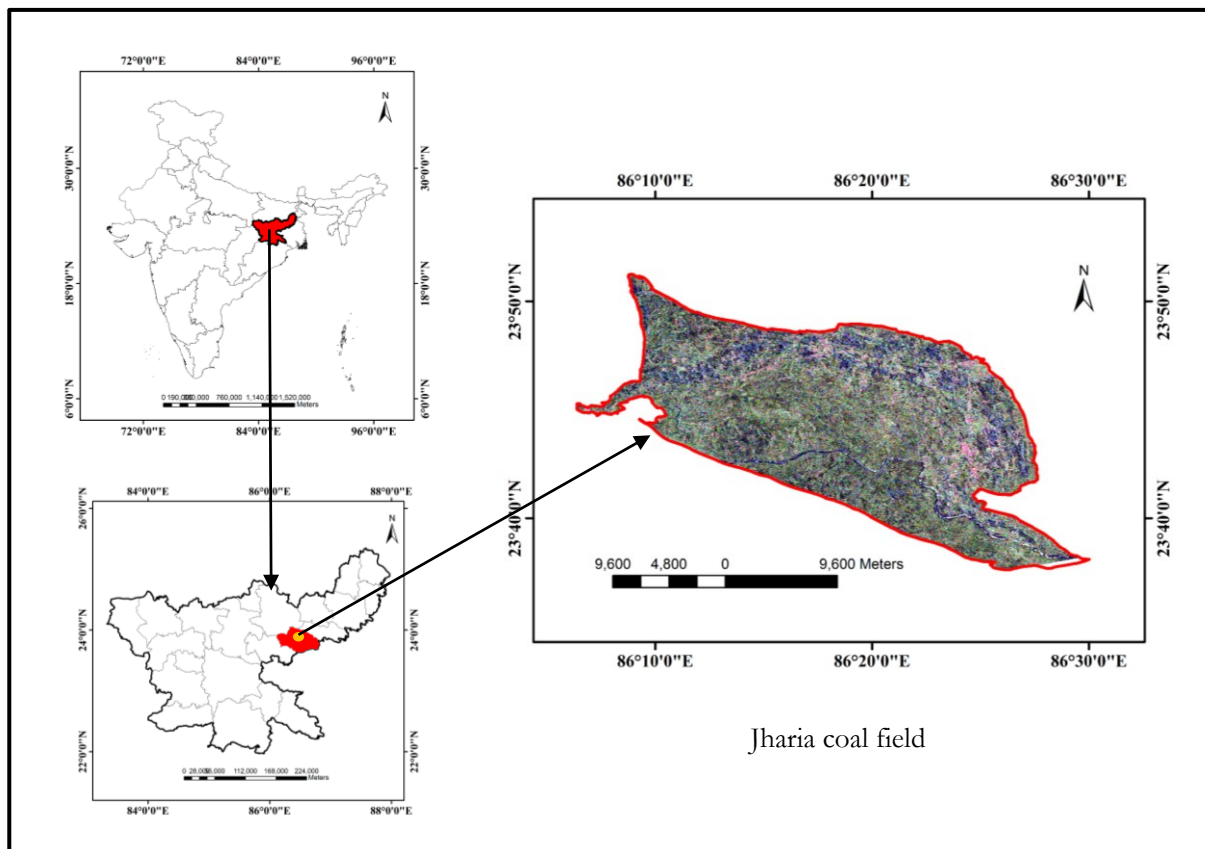


Figure 4: Study area Jharia coal field from SAR (Pauli RGB image, R: HH-VV; G: HV; B: HH-VV) images and the red line represents the shape file of the study area.

4.2. Dataset used

4.2.1. RADARSAT 2 data

Identification of opencast mining indicators and their properties was done from Radarsat 2 satellite images acquired on dated 28th November 2010 and 23rd November 2011 in the Jharia coal field area. Radarsat 2 imagery operate in C-band, wavelength 5.6 cm. The fully polarimetric data provides better information about the identification of surface scatterers that's why fully polarimetric data is chosen for the present research.

Table 1: Specification of Polarimetric SAR data used

Specification	Radarsat 2	
	28/11/2010	23/11/2011
Date of acquisition	28/11/2010	23/11/2011
Wavelength	C band 5.6 cm	C band 5.6 cm
Spatial resolution	Pixel spacing – 4.733m Line spacing – 4.7779m	Pixel spacing – 4.733m Line spacing – 4.7363m
Incidence angle	Near range – 26.8441° Far range – 28.6585°	Near range – 25.6845° Far range – 27.5282°
Polarimetric mode	HH, HV, VH, VV	HH, HV, VH, VV
Satellite Passes	Ascending	Ascending

4.2.2. ENVISAT ASAR data

ENVISAT is an advanced polar-orbiting Earth observation satellite. ENVISAT provides measurements of atmosphere, ocean, land and ice. ASAR is advanced synthetic aperture radar operates in the C band.

Time series polarimetric data of ENVISAT ASAR is chosen for land deformation monitoring from 17th March 2007 to 10th April 2010.

Acquisition incidence angle is 22.8559°, wavelength is 5.6236 cm and ascending satellite passes. Following table shows the other relevant specification of single polarised SAR data from ENVISAT ASAR satellite.

Table 2: Specification of single polarised SAR data used.

Sl. No.	Date of Acquisition (YYYYMMDD)	Polarisation	Perpendicular baseline in m w.r.t. master image (Sl. No 13)	Temporal baseline in day w.r.t. master image (Sl. No 13)
1	20070317	VV	-335.311742	-629.999930
2	20070421	VV	-74.378710	-594.999932
3	20070526	VV	-31.051206	-559.999907
4	20070630	VV	-61.825527	-524.999893
5	20070804	VV	46.648789	-489.999890
6	20070908	VV	-195.497305	-454.999917
7	20071013	VV	105.634409	-419.999944
8	20071117	VV	-276.741575	-384.999966
9	20071222	VV	259.343520	-349.999974
10	20080301	VV	228.120788	-279.999969
11	20080614	VV	-197.795103	-174.999959
12	20080927	VV	80.697844	-69.999993
13	20081206	VV	0.000000	0.000000
14	20090110	VV	-46.392948	34.999992
15	20090214	VV	-144.070467	70.000002
16	20090704	VV	-97.269870	210.000022
17	20091226	VV	39.594480	384.999940
18	20100130	VV	-288.627223	419.999942
19	20100306	VV	33.076738	454.999935
20	20100410	VV	-193.778981	489.999927

4.3. Tools used

Some softwares are present to process fully Polarimetric SAR and Single polarised SAR data. In this study PolSARpro, version 5.0 was used for processing of PolSAR data. Another software, SARPROZ was used for time series single polarised SAR data processing to generate land deformation information. ENVI and ArcGIS software were used for image processing. MATLAB software was used for discrete wavelet based image fusion. R software was used for polarisation orientation angle estimation and histogram generation.

4.4. Data for Validation

Ground truth data was collected during December, 2011. Validation of results were done based on the ground truth data was collected. Table 3 represents the summary of ground truth data.

Table 3: Summary of ground truth data

S.N.	Name of features	Number of features present (approx.)
1	HEMM and opencast active mining face	22
2	Water body within opencast mine	3
3	Coal storage	1
4	View point	6

Following image shows the ground truth data location of various mining features including HEMM over an LISS-IV data of Jharia coalfield.

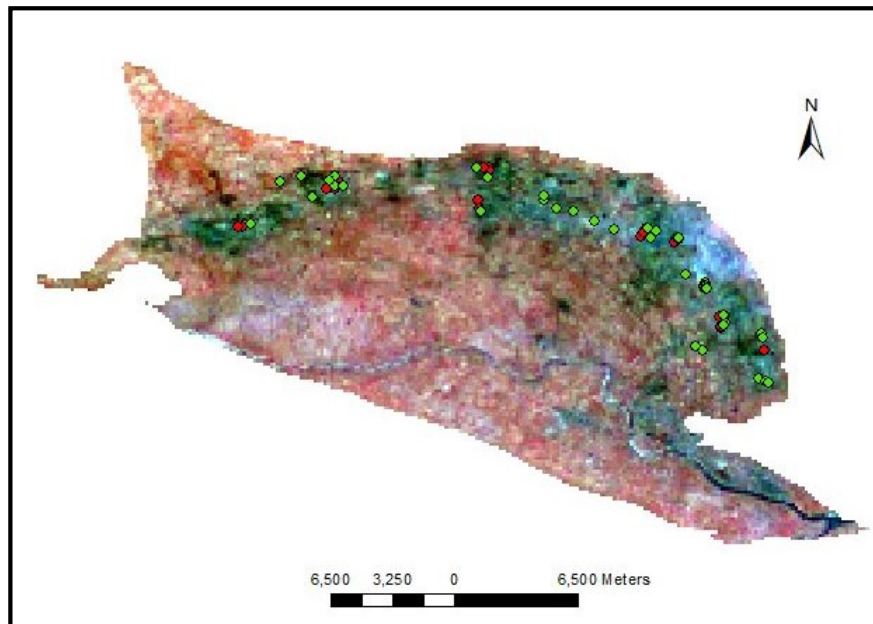


Figure 5: Red point represents HEMM and green point represents other than HEMM of ground truth data in LISS IV image of Jharia coal field.

A red pixel represents the location of HEMM ground truth data in LISS IV image of Jharia coal field. A green pixel represents the location of ground truth data of other than HEMM. Validation of result was done by using the ground truth data.

5. RESEARCH METHODOLOGY

The purpose of this research is to identify opencast mining indicators and their properties and time series PSInSAR based land deformation. Combine the time series land deformation information with responsible mining indicators and their properties to find out the spatial relationship among them. To achieve these goals, the following methodology as shown in figure 6 was adopted. Initially, multi-polarisation SAR data was processed and various polarimetric properties i.e. single bounce scattering, double bounce scattering, volume scattering, helix scattering, entropy, and anisotropy information was extracted. Based on polarimetric properties, classification of mining indicators was accomplished. Next, time series of single polarised SAR images were processed to generate land deformation information. Then, integration of both the information was done by using discrete wavelet fusion operation.

5.1. Research workflow

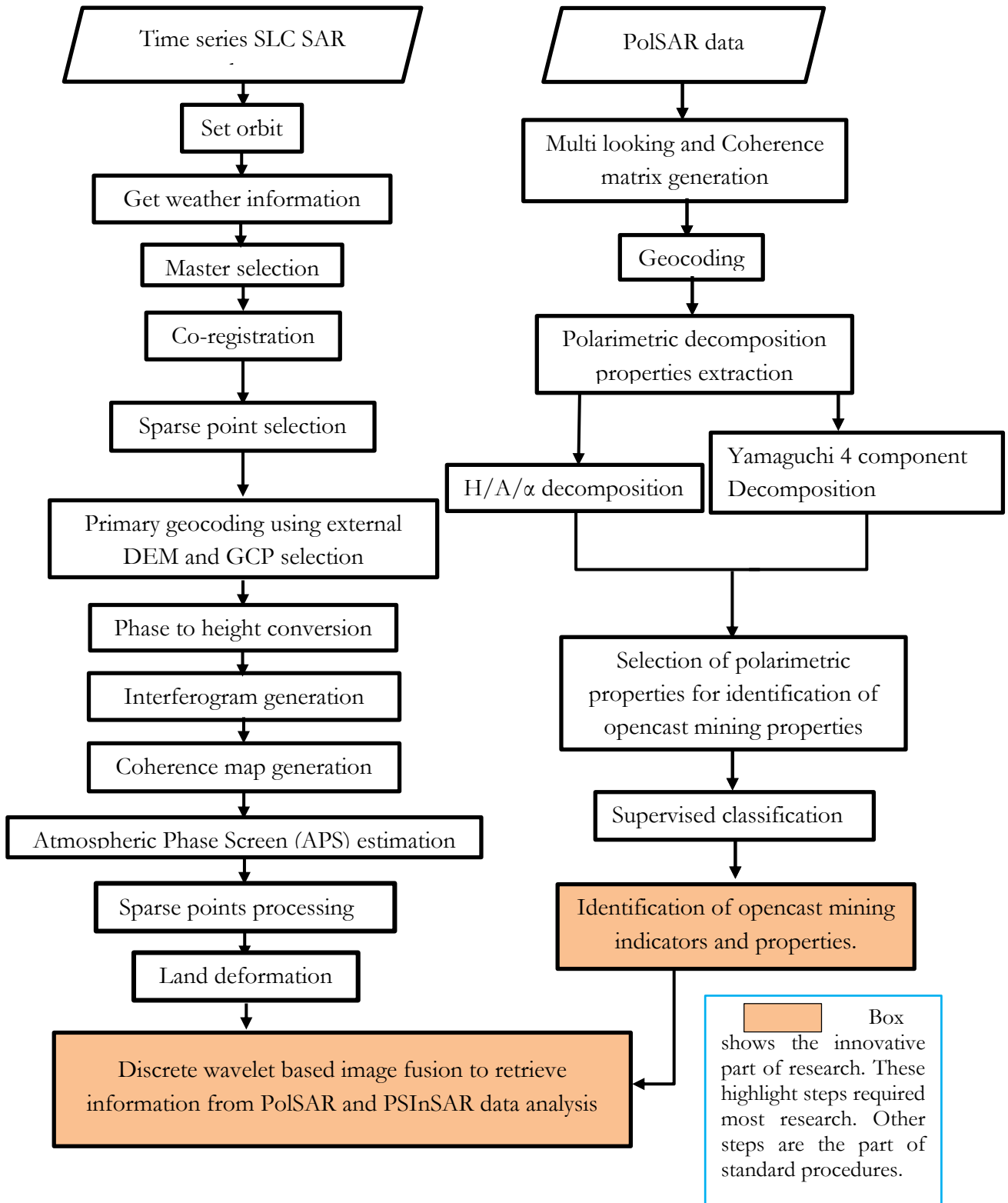


Figure 6: Flow chart

SAR data acquire in radar coordinate system and is measured in slant range resolution. So, SAR data was converted from slant to ground range by using the following formula.

$$\text{Ground range} = \frac{\text{Slant range}}{\sin \tilde{\theta}} \quad (5.1)$$

Where, $\tilde{\theta}$ = Incidence angle.

5.2. Polarisation orientation angle shift in PolSAR data

5.2.1. Estimation of polarisation orientation angle shift

The polarisation orientation angle shift (θ in degree) in PolSAR data was estimated by using the following equation

$$\theta = \eta, \quad \text{if } \eta \leq 45^\circ \quad (5.2)$$

$$\theta = \eta - 90^\circ, \quad \text{if } \eta > 45^\circ \quad (5.3)$$

Where,

$$\eta = \frac{1}{4} \left[\tan^{-1} \left(\frac{-4\text{Re}(\langle (S_{HH} - S_{VV})S_{HV}^* \rangle)}{-\langle |S_{HH}|^2 - |S_{VV}|^2 \rangle + 4\langle |S_{HV}|^2 \rangle} \right) + 180^\circ \right] \quad (5.4)$$

5.2.2. Deorientation

The coherency matrix was rotated by the mean estimated orientation angle (θ) along the radar line of sight

$$[T_3(\theta)] = [R_3(\theta)][T][R_3(\theta)]^{-1} \quad (5.5)$$

Where, $R_3(\theta)$ is the special unitary rotation operator, is expressed by as follows

$$[R_3(\theta)] = \begin{bmatrix} 1 & 0 & 0 \\ 0 & \cos 2\theta & \sin 2\theta \\ 0 & -\sin 2\theta & \cos 2\theta \end{bmatrix} \quad (5.6)$$

After the rotation by the mean estimated orientation angle (θ), the element of coherency matrix T_3 becomes

$$[T_3(\theta)] = \begin{bmatrix} T_{11}(\theta) & T_{12}(\theta) & T_{13}(\theta) \\ T_{21}(\theta) & T_{22}(\theta) & T_{23}(\theta) \\ T_{31}(\theta) & T_{23}(\theta) & T_{33}(\theta) \end{bmatrix} \quad (5.7)$$

5.3. PolSAR data processing for identification of various opencast mining indicators

Identification of various opencast mine properties or equipment to identify mine properties was done from fully polarimetric SLC SAR data. Multi-look and coherency matrix had been generated from the fully polarised data. Then map projection system and pixel size (resampling) had been defined in map ready tool. Yamaguchi four component decomposition and H/A/ α decomposition had been applied after defining map projection. Therefore, Yamaguchi four component decomposition of the coherency matrix of the incoherent type was decomposed as single bounce scattering, double bounce scattering, volume scattering and helix scattering. H/A/ α decomposition of the coherency matrix decomposed as entropy, anisotropy, and alpha. Standardisation of each decomposed scene was performed which ranges pixels value from zero (0) to one (1) in a particular scene. Selection of polarimetric properties for identification of opencast mining

properties was done. After that layer stacking operation had been performed which generated 6 bands image. The selected bands were single bounce scattering, double bounce scattering, volume scattering, helix scattering, entropy, and anisotropy value. The training set was prepared for each mining feature after considering the polarimetric responses of each pixel and then band statistics was calculated. Band statistics gave an idea about most suitable polarimetric properties to identify mining indicators and their properties. After that, supervised classification technique was used to classify mining features. Identification of various mine properties or features was done on the result obtained from Yamaguchi decomposition and H/A/ α decomposition.

5.4. Mining properties identification

Opencast mine has some unique geometric structure such as plane surface, dihedral plane and some association property which give particular polarimetric responses depending upon the wavelength of radar pulses as follows.

The bottom surface of opencast mine can be identified by single bounce scattering whereas benches can be identified by the double bounce scattering of PolSAR data.

HEMM are operated within the opencast active mining faces. So, active mining faces were identified by HEMM considering the association property with active mining faces. Abandoned mine was identified by the water accumulation in the bottom surface of an opencast mine whereas bottom surface of active opencast mine was dry in nature.

Identification of various mining properties was done based on their polarimetric responses. Some of the polarimetric responses may change based on the wavelength of incident radar pulses. Variation of polarimetric responses came from same mining properties from various opencast mines observed due to various stages of opencast mine such as some mines were new and well maintained of mine geometry (Block 2 opencast mine shown in Figure 7), not abandoned mine however not well maintained of mine geometry (Chasnala opencast mine shown in Figure 7), and abandoned mine (Basdeopur 2 opencast mine shown in Figure 7).

Therefore, four opencast mines such as Block 2, Tata Sijua, Basdeopur, and Chasnala was selected to maintain the variability of polarimetric responses for identification of mining indicators and their properties in training set data. HEMM pixels were selected from various other opencast mines including the above mentioned opencast mines. Figure 77 shows the location of four opencast mines such as Block 2, Tata Sijua, Basdeopur, and Chasnala represented by 1, 2, 3, and 4 respectively. Following Table 5 shows the various polarimetric responses of various mining properties.

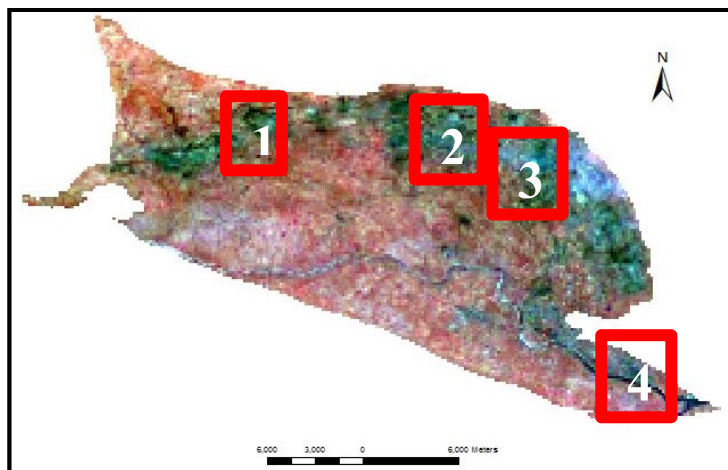


Figure 7: Location of four opencast mines within study area

5.4.1. Identification of HEMM based on entropy value and double bounce value

$H < 0.3$ including double bounce pixel value (>0.01) represent coherent structure such as HEMM (metallic object) within opencast mine premises. Entropy (H) scene and double bounce scene were generated from coherency matrix of fully polarimetric data of study area by using standard H/A/ α decomposition and Yamaguchi decomposition, respectively. $H < 0.3$ including double bounce value (>0.01) in a pixel were identified within the opencast mine area. The training set of HEMM was created and band statistics was calculated in ENVI classic image processing software. The supervised classification was performed to identify HEMM pixels. Pixels identified within the opencast mine area was considered as HEMM.

First, fully polarimetric SAR scene of 23rd November 2011 was selected for identification of HEMM pixel and validation of HEMM pixel was performed with ground truth data acquired in December 2011.

Then, the similar classification was performed in fully polarimetric SAR scene of 28th November 2010 to identify HEMM in opencast mine.

5.4.2. Opencast active mine faces

HEMM are operated in the opencast active mine faces. The position of HEMM within opencast mine area symbolise that excavation is in progress in that place. So, identification of opencast active mining faces were done based on the location of HEMM identified in the opencast mine area.

5.4.3. Characteristic of opencast mine floor filled with water

Water body generates low backscatter value and appear in black colour in RGB image when visualise double bounce scattering in red band (R), volume scattering in green band (G) and single bounce scattering in blue band (B). The training set was prepared based on water present within the opencast query. Time series Google earth images were also considered to identify correct training sample. The classification was performed to find out another water body within study area based on the prepared training set. Opencast mine floor filled with water represents abandoned mines or no mineral extraction is in progress.

5.4.4. Characteristic of opencast mine floor mixture with soil and rock

Active opencast mines are those where mineral extraction are going on. In the case of active opencast mine, the opencast mine floors are not filled with water. Generally, active opencast mine floor contains a mixture of soil and rock. A training set of opencast mine floor mixture of soil and rock was prepared based on high single bounce polarimetric response and with the help of Google earth image. The classification was performed to identify opencast mine floor mixture with soil and rock, without water.

5.4.5. Characteristic of bench and terrace

Benches and terraces of opencast mines have dihedral geometric structure. Dihedral geometric property predominantly generates high double-bounce scattering. So, benches and terraces were identified by higher double bounce pixels within opencast mine area in the PolSAR scene. The classification was performed based on prepared training set to identify benches and terraces in the opencast mine area.

5.4.6. Mass wasting phenomena

Mainly, randomly scattered various dimensional loose rocks are present in the case of mass wasting. So, mass wasting area generates high volume scattering. Therefore, training set of mass wasting phenomena was prepared based on high volume scattering pixel and with the help of Google earth image of opencast mine area. Finally, the classification was performed to identify mass wasting phenomena within opencast mine.

5.4.7. Characteristic of opencast rim area

Fault zone or fracture zone can be identified from volume scattering only if, opencast rim area is a barren land i.e. not covered with vegetation, forest, and urban area. Residential areas presented around the opencast mine and some of the area was also covered with forest in this study area. Identification of small fault zone or fracture zone is also difficult in $10\text{m} \times 10\text{m}$ pixels size.

Training sets were prepared for HEMM, opencast mine floor, opencast mine water, mass wasting area, benches and terraces based on the identification of opencast mining properties in PolSAR data with the help of Google earth images. Supervised classification of mining area was performed based on the training set.

5.5. PSInSAR processing

20 ENVISAT ASAR time series (17th March 2007 to 10th April 2010) SLC data was selected for identification of land deformation in Jharia coalfield by using permanent scatterers InSAR processing. Before, selecting the polarisation, the set orbit option was selected to read the orbit information of each SLC data. After that automatic master image was selected after considered the coherence value of 0.5 among the data set. Then, initially, the approximate centre coordinate of study area including the radius of the study area was selected for performing land deformation. After that master extraction, slave extraction, and co-registration was performed respectively. Site processing option was selected. Preliminary analysis was performed first, next, preliminary geocoding was performed. Then, InSAR processing was performed. After that, multi-image InSAR processing was done by considering coherence of 0.65 as a threshold. Finally, sparse point selection and sparse geocoding were done to visualise land deformation information.

5.6. Integrated information obtained from PolSAR and PSInSAR data analysis and visualisation

Classified opencast mining indicator and their properties were generated from PolSAR data. Land deformation information was generated from single polarised time series SAR data. Discrete wavelet based image fusion operation was performed to retrieve spatial relation between classified opencast mining properties and land deformation information.

Discrete wavelet transform technique was used to decompose each image. In this technique, an image is converted from spatial domain to frequency domain. In first level, each image was decomposed into low – low, low –high, high-low, high –high frequency components by discrete wavelet transform technique. In the second level low – low frequency component of the first level was considered as input and was decomposed into four components, similar to the first level. Wavelet coefficients were generated when discrete wavelet transform technique applied on the source image. The average of wavelet coefficients of both the input decomposed images were used to generate fused image in the inverse discrete wavelet transform technique. So that, low frequency and high frequency were preserved in the output fused image. Changes of land deformation with respect to mining properties were evaluated. A simple 3D (X, Y, and colour) visualisation was performed to envisage the nature and intensity of land deformation with respect to opencast mining indicators and their properties. Identification, monitoring and characterisation of opencast induced land deformation were done by using integrated information obtained from PolSAR and PSInSAR data analysis.

6. RESULTS

6.1. Estimation of Polarisation orientation angle shift (θ)

6.1.1. 2011 PolSAR scene

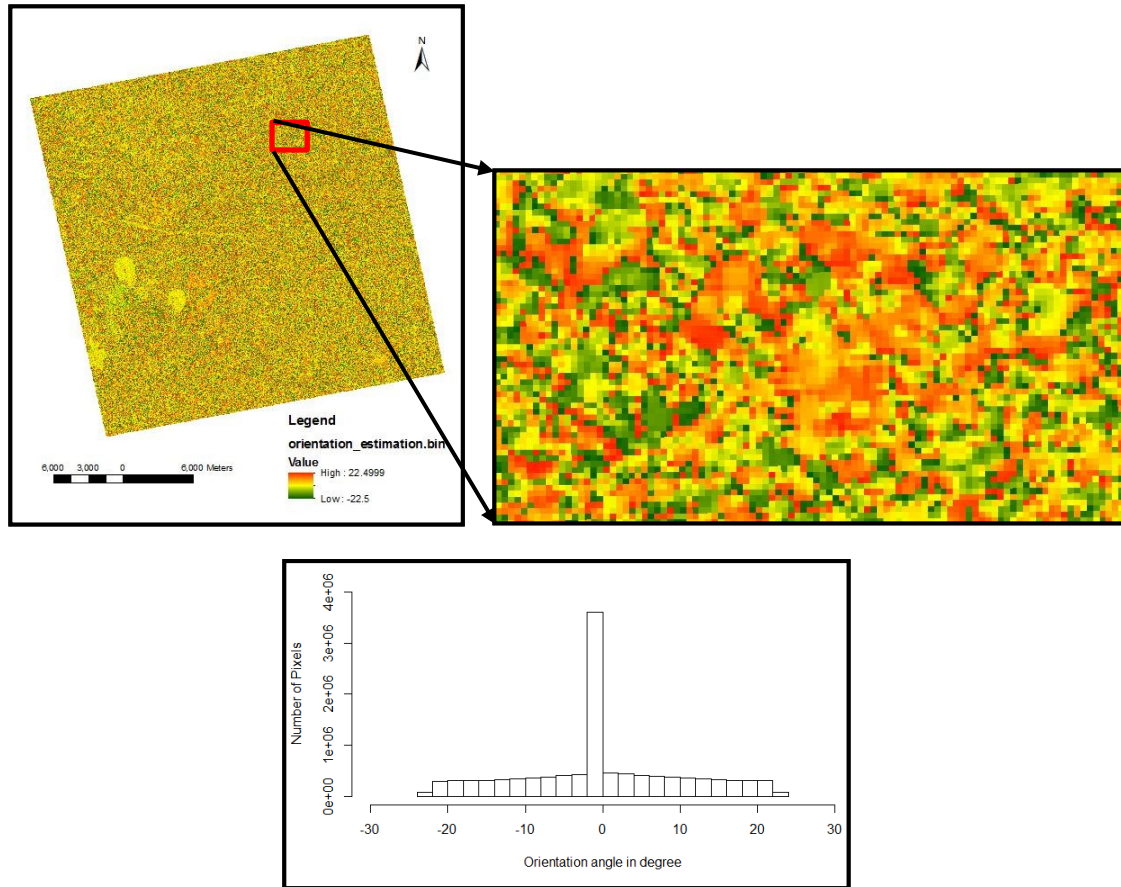


Figure 8: Polarisation orientation angle shift (θ in degree) estimation of 2011 scene (left image), zoom of mining area (right image) and a histogram of polarisation orientation angle shift estimation (below image).

The mean estimated orientation angle shift is 0.079° for 23rd November 2011 PolSAR scene.

The effect of polarisation orientation angle shift was observed higher on opencast mine topography shown in zoom of mining area of Figure 8 and 9. The polarisation orientation angle shift was observed mainly positive in opencast mine area.

6.1.2. 2010 PolSAR scene

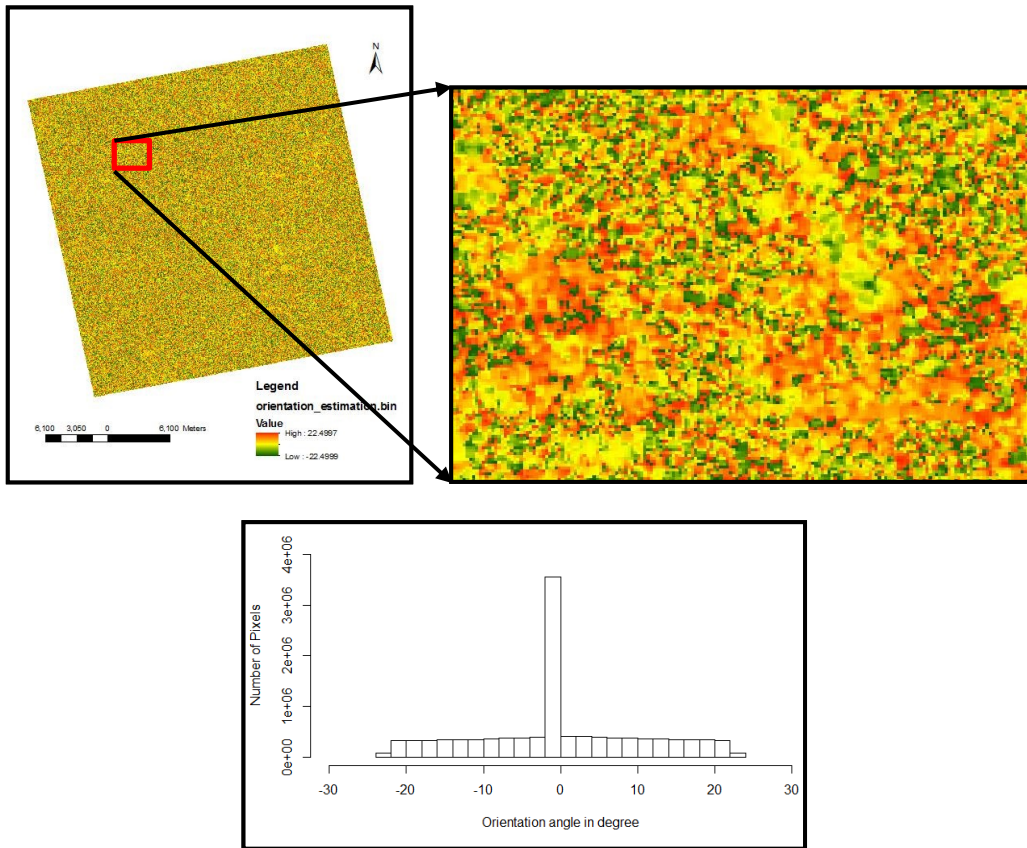


Figure 9: Polarisation orientation angle shift (θ in degree) estimation of 2010 scene (left image), zoom of mining area (right image) and a histogram of polarisation orientation angle shift estimation (below image)

The mean estimated orientation angle shift is 0.072° for 28th November 2010 PolSAR scene.

Table 4: Effect of polarisation orientation angle shift on the elements of coherency matrix.

SAR scene	Before deorientation (mean)		After deorientation (mean)		Remarks
	2010 scene	2011 scene	2010 scene	2011 scene	
T_{11}	0.1705755	0.1813068	0.1705755	0.1813068	Equal
T_{22}	0.05928647	0.06845976	0.06052453	0.07037433	Increase
T_{33}	0.04554954	0.04676434	0.04431148	0.04484978	Decrease
T_{12} real	0.01185275	0.01562003	0.0113908	0.0156117	Small decrease
T_{12} imaginary	-0.0003427	-0.0024968	-0.000189	-0.001559	Small decrease
T_{13} real	0.00070846	-0.0003433	0.0003367	-0.000869	Small change
T_{13} imaginary	-0.0008082	-0.0025976	-0.000827	-0.002442	Small change
T_{23} real	0.00171938	0.00254982	-8.06e-05	-9.033e-05	Close to zero
T_{23} imaginary	-2.881e-05	-0.0001991	-2.881e-05	-0.0001991	Equal

6.2. Polarimetric responses of mining properties

Following Table 5 shows the polarimetric responses such as single bounce, double bounce, volume scattering, helix scattering, entropy value and anisotropy value with respect to various mining properties such as HEMM, opencast mine floor mixture with soil and rock without water, opencast mine floor filled with mine water, benches and terraces, and mass wasting phenomena.

Table 5: Mining indicators and their polarimetric responses

Mining Indicators		Single bounce	Double bounce	Volume scattering	Helix	Entropy	Anisotropy	Remarks
HEMM from 2011 scene		0.005± 0.004	0.123± 0.096	0.003± 0.005	0.016± 0.041	0.212± 0.064	0.613± 0.171	Identification of active mining faces has been done from location of HEMM in an opencast mine.
HEMM from 2010 scene		0.024± 0.048	0.096± 0.099	0.001± 0.001	0.003± 0.004	0.239 ± 0.057	0.633 ± 0.145	
Opencast floor can be divided as follows	Water accumulated means abandoned mines	0.0008 ± 0.0009	0.0001 ± 0.0001	0.0001 ± 0.0001	0.0002 ± 0.0003	0.683 ± 0.157	0.493 ± 0.140	Intensity is low compare to Smooth no stagnant water accumulated
	Mixture of soil and rock (rough surface) no accumulated stagnant water means active mines	0.006 ± 0.004	0.0001 ± 0.0001	0.001 ± 0.001	0.001 ± 0.001	0.512 ± 0.152	0.413 ± 0.142	Intensity high compares to Water accumulated means abandoned mines
Bench (B) and terrace (H)		0.015± 0.018	0.002± 0.004	0.002 ± 0.002	0.002± 0.002	0.561± 0.133	0.461 ± 0.185	Solid rock presents in the benches.
Opencast slope properties. Slope morphology includes the followings:	Overall slope angle							Almost constant; overall slope angle varies within a limit for a specific opencast mine.
	Presence of fracture							Very difficult to identify in the 10m pixel size.
	Mass wasting phenomena	0.0003 ± 0.0005	0.0000 ± 0.0001	0.003 ± 0.0008	0.003 ± 0.002	0.768 ± 0.109	0.464 ± 0.171	Loose rocks give higher volume scattering than double bounce.

Graphical representation of polarimetric responses of various mining properties

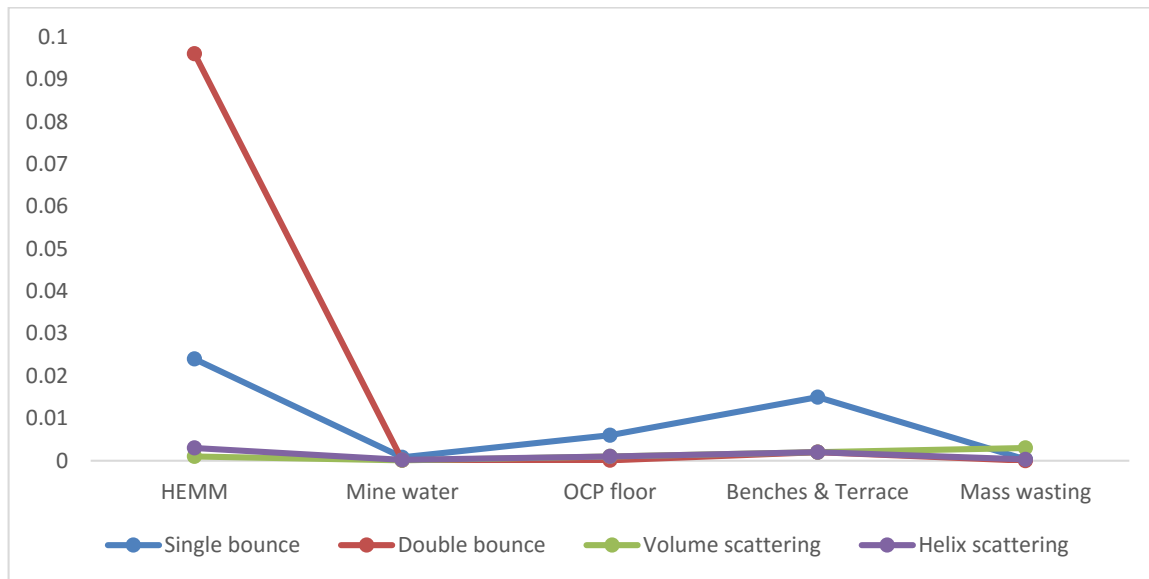


Figure 10: Yamaguchi Polarimetric responses of various mining properties



Figure 11: Entropy and Anisotropy responses of various mining properties

HEMM generated high double bounce value, mine water gave high single bounce polarimetric response, opencast mine floor generated higher single bounce than mine water, benches and terraces gave high single bounce including second highest double bounce and mass wasting generated high volume scattering shown in Figure 10. The various value of entropy and anisotropy polarimetric responses of various mining indicators and their properties shown in Figure 11.

6.3. Identification of HEMM

6.3.1. Based on entropy value and double bounce

Training set to identify HEMM was created based on entropy pixel value < 0.30 and double bounce pixel value > 0.01 . The figure 12 shows the HEMM points (shown as green points) identified based on polarimetric properties of 2011 scene shown in the LISS-IV image.

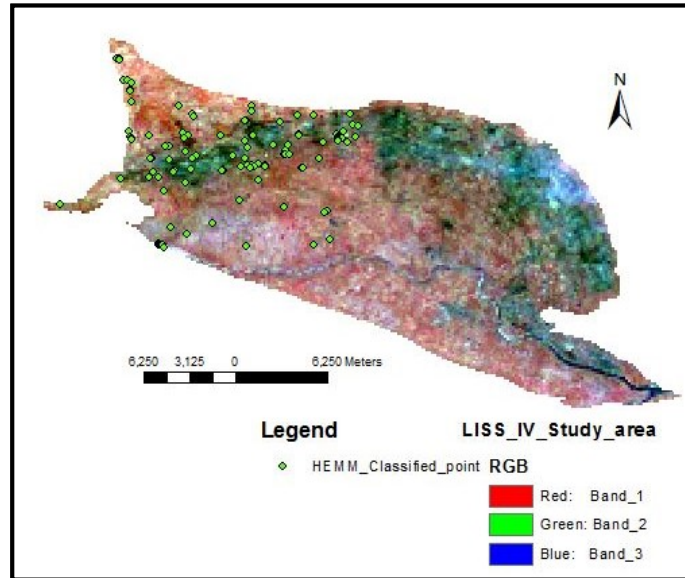


Figure 12: Green point represents classified HEMM shown in LISS IV image of study area

Validation of HEMM pixels shown in figure 13.

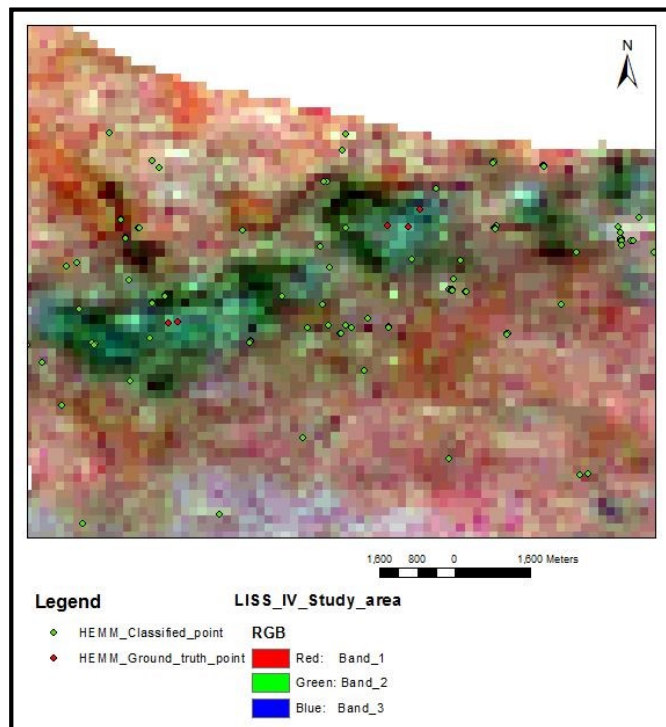


Figure 13: Red point represents ground truth and green point represents classified points of HEMM shown in the LISS-IV image.

Two fully polarimetric SAR scenes were available of which, one was acquired on 23rd November 2011 and the other was acquired on 28th November 2010. The ground truth data was collected in December 2011. So, validation by using ground truth data is justified for 23rd November 2011 SAR scene. Identification of HEMM pixels from fully polarimetric SAR data was possible and validation of results was done by using the available five points of ground truth data of HEMM. Red points represent the ground truth data received from the field and green points indicate classified HEMMs generated from fully polarimetric SAR scene dated 23rd November 2011, as shown in Figure 133. However, four out of five ground truth points are located at a distance of about 350 m from the nearest classified HEMM points.

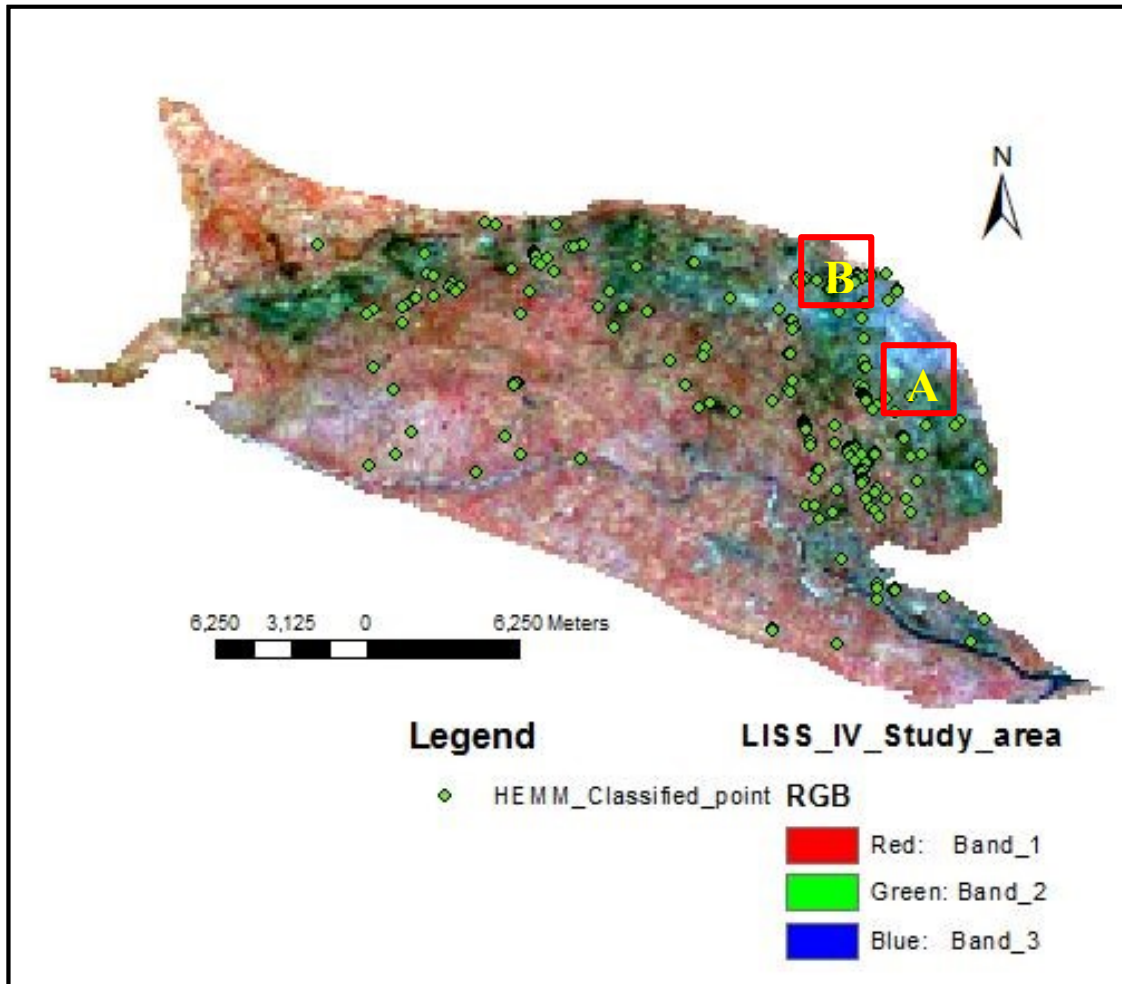


Figure 14: Green points represents classified HEMM overlay on LISS-IV image.

Green points shown in Figure 144 represent the HEMM responses. All green points are shown in Figure 122, Figure 143 and Figure 14 are not represented as HEMM. There are some points which have similar polarimetric responses like HEMM and classified as HEMM but have mostly come from the urban area. However, the classified HEMM points that do not come from opencast mine area, are not represented as HEMM in the study. Two zoom areas are selected, which are shown in red rectangle boxes and name as “A” and “B” in Figure 145. The Google earth image of the zoom area of “A” and “B” (in Figure 15) are shown in Figure 15A-B.

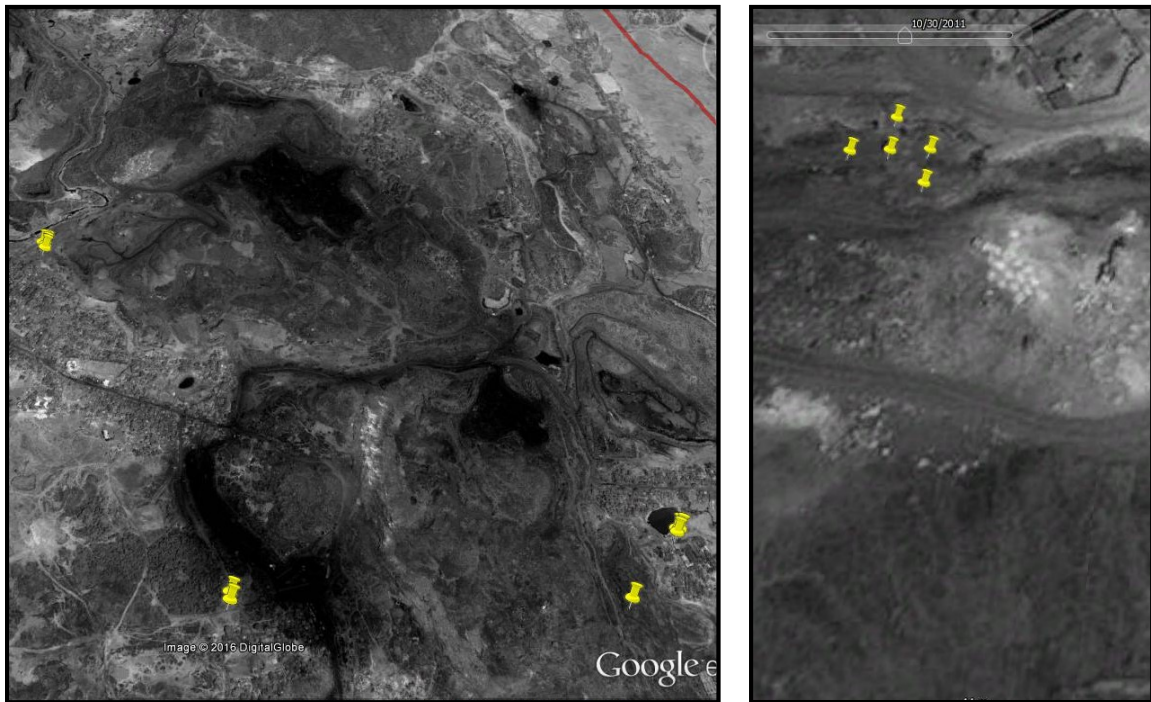


Figure 15: A - B HEMM classified image shown in Google earth image dated 30th October 2011

Yellow icons represent the HEMM pixels shown in Figure 155 A-B. Fully polarimetric data was acquired on 28th November, 2010; plotted the classified HEMM points on Google earth image dated 30th October 2011 shown in Figure 15 A-B. The position of HEMM pixels (yellow icon in the images) within the opencast mine represents the location of active faces of opencast mine shown in Figure 165 A-B.

6.4. Identification of active mining faces

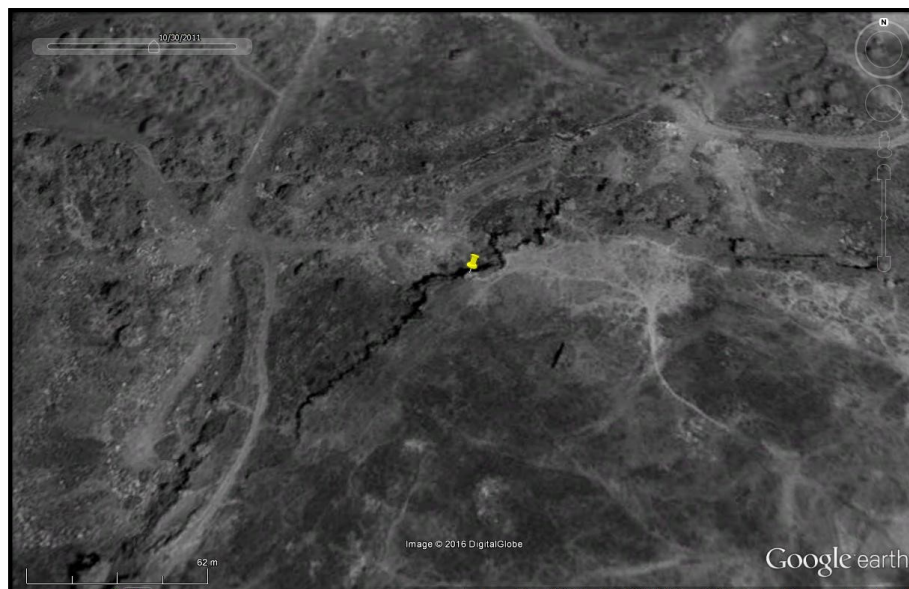


Figure 16: Identification of active opencast mine faces from HEMM location
The HEMM worked on an opencast active mine face which is clearly visible in Figure 16.

6.5. Identification of opencast mining properties

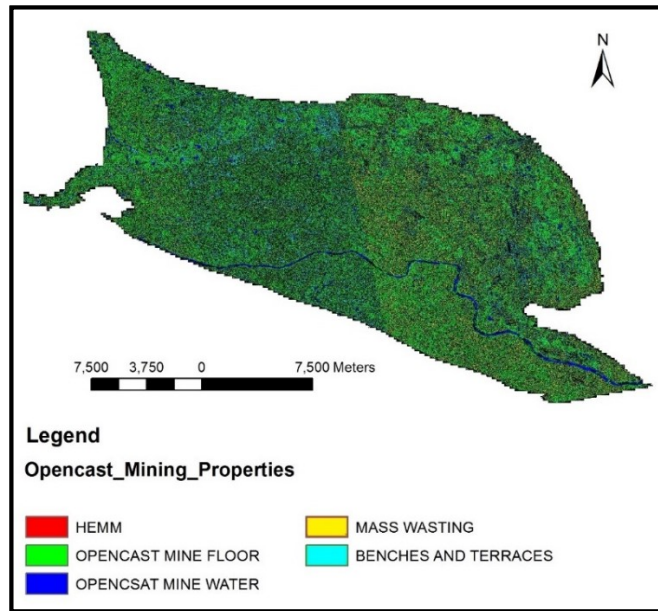


Figure 17: Classified image of opencast mining properties

Classified image of opencast mining properties is shown in Figure 17. In Figure 17 HEMM, opencast mine floor without water, opencast mine water, mass wasting area, and benches and terraces represented by red, green, blue, yellow and cyan colour pixel, respectively. Some zoom area of the classified image of mining properties (shown in Figure 17) have been shown below (shown in Figure 178 - 21) where the legend is similar to the classified image of mining properties of Figure 17.

6.5.1. Identification of opencast floor mixture with of soil and rock with no accumulated stagnant water

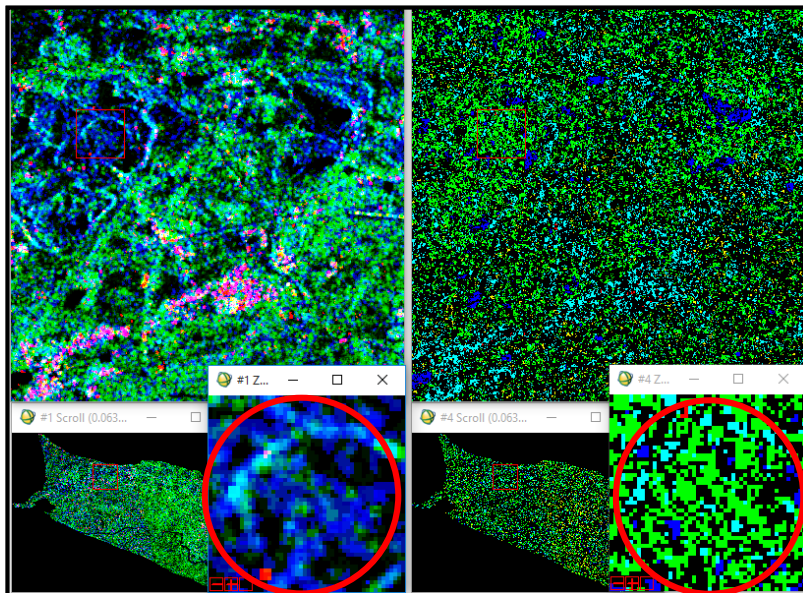


Figure 18: Opencast floor mixture with of soil and rock with no accumulated stagnant water

Left side image of Figure 18 visualised in RGB band where double bounce viewed in red band (R); volume scattering viewed in green band (G) and single bounce viewed in blue band (B). Right side image of Figure 18 is a classified image of various opencast mine properties. Opencast mine floor mixture with soil and rock

is shown in zoom window of both (left and right) the images of Figure 18. The red circle shown in Figure 18, encircled the opencast mine floor. Opencast mine floor mixture with soil and rock without water was identified in Figure 18.

6.5.2. Identification of opencast floor filled with water

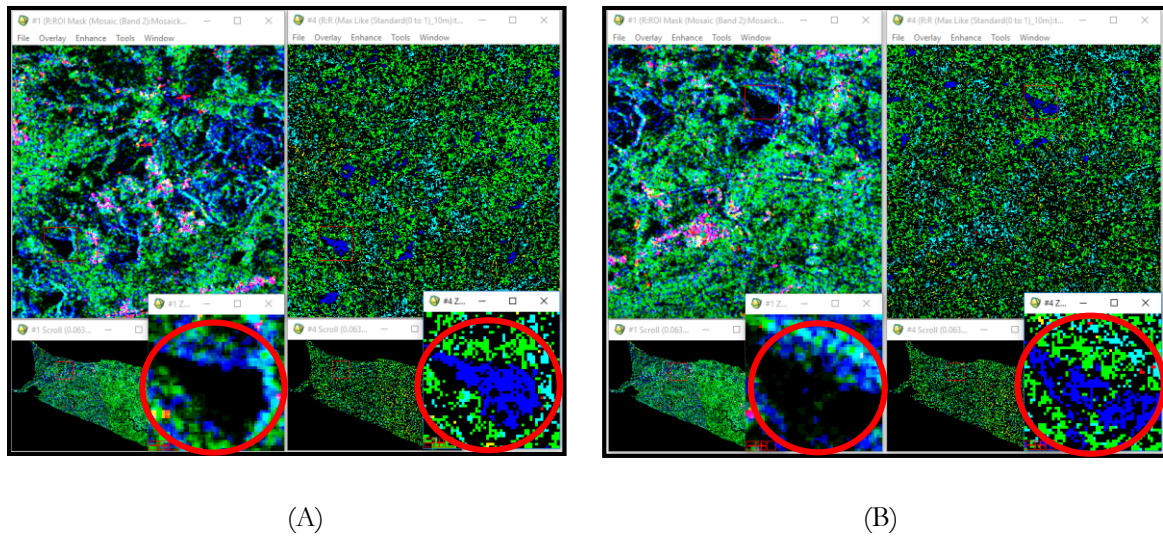


Figure 19: Opencast mine floor filled with water

Left side image of Figure 19A and 19B is same left side image as shown in Figure 18. The backscatters value is low in case of the water body. Water body of opencast mine appears as black colour in an RGB image of SAR scene when double bounce visualises in red band (R); volume scattering visualises in green band (G) and single bounce visualises in blue band (B). The zoom window shows the opencast mine water which is also encircled by a red circle. Opencast mine water was clearly identified in the classified zoom image window of right side image of Figure 19A and 19B.

6.5.3. Characteristic of benches and terrace

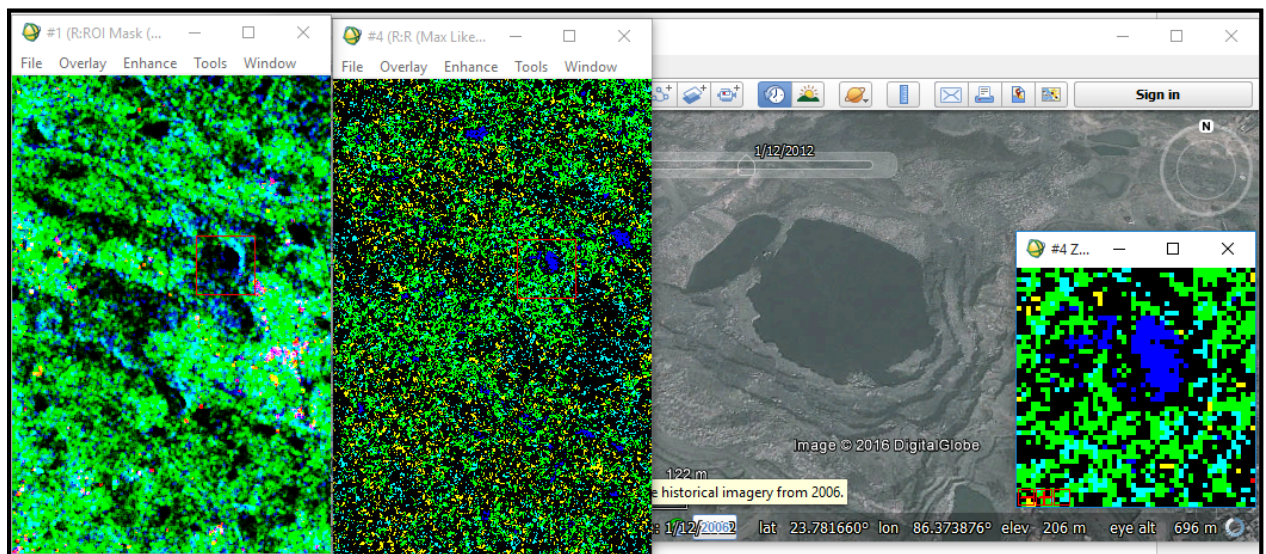


Figure 20: Benches and terraces identified in classified image

Figure 20 divided into 4 sub frames. Second sub frame (from left) is a classified image of mining properties and first sub frame image (from left) is before classification. Third sub frame (from left) is Google earth image and the 4th sub frame is zoom area of the classified image. Benches and terraces were identified and highlighted in the cyan colour pixels shown in zoom image. The validation of result was done from Google earth image shown in Figure 20.

6.5.4. Mass wasting phenomena

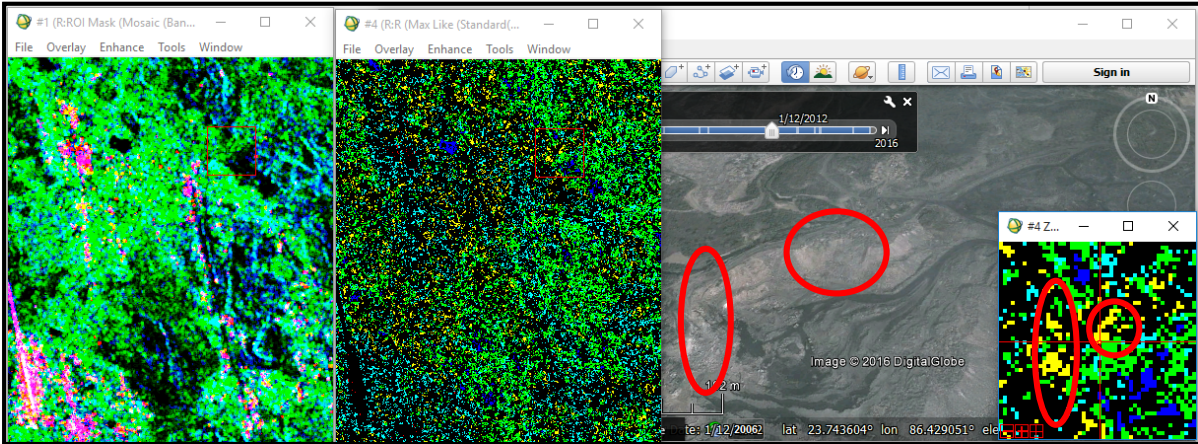


Figure 21: Classification image of mass wasting phenomena

Figure 21 is divided into four sub frames and the sub frames are similar to Figure 20. Red ellipses show the area of mass wasting within opencast mine. The validation of result was done from Google earth image shown in Figure 21.

6.6. Land deformation information from PSInSAR technique

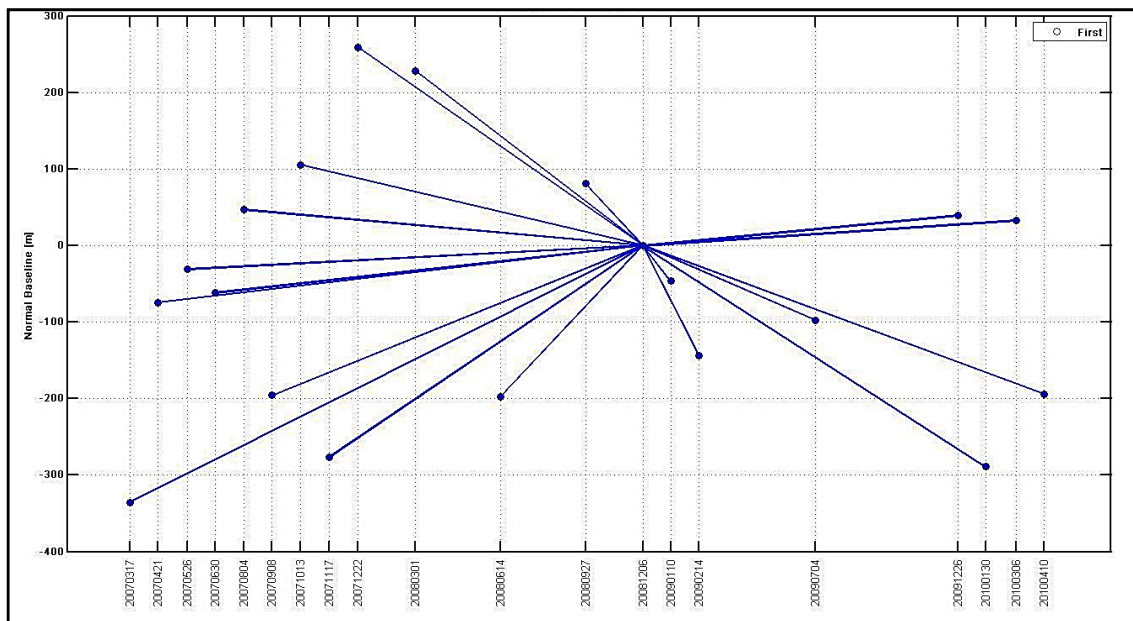


Figure 22: Normal baseline distance in m in the Y axis, the temporal extent in the X axis of 20 numbers of time series ENVISAT data and coherence threshold 0.5.

20 single polarised SAR data set were selected to generate the trend of land deformation. Among them, 06th December 2008 scene was considered as master image and others were considered as slaves. Acquisition date or temporal distance in day in X axis and normal baseline distance in m in Y axis of data set shown in Figure 22. First nine ENVISAT data (older from acquisition date wise) have low temporal distance, however, normal baseline varies from -350 m to 300 m shown in Figure 22. The rest of the ENVISAT data have less normal baseline variability and high temporal variability compares to first 9 ENVISAT data shown in Figure 22. Coherence threshold was selected to 0.5 for the selection of master data.

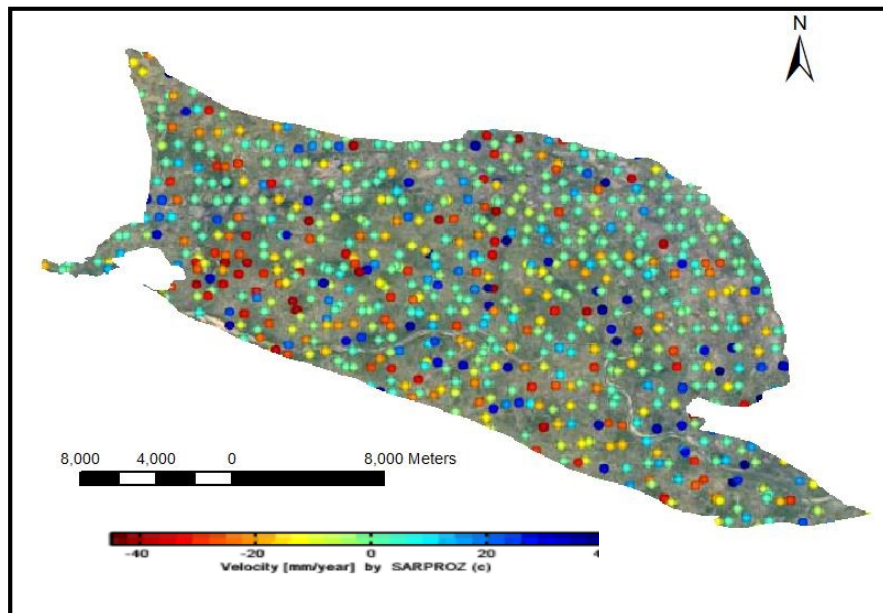


Figure 23: Land deformation information in Google Earth image

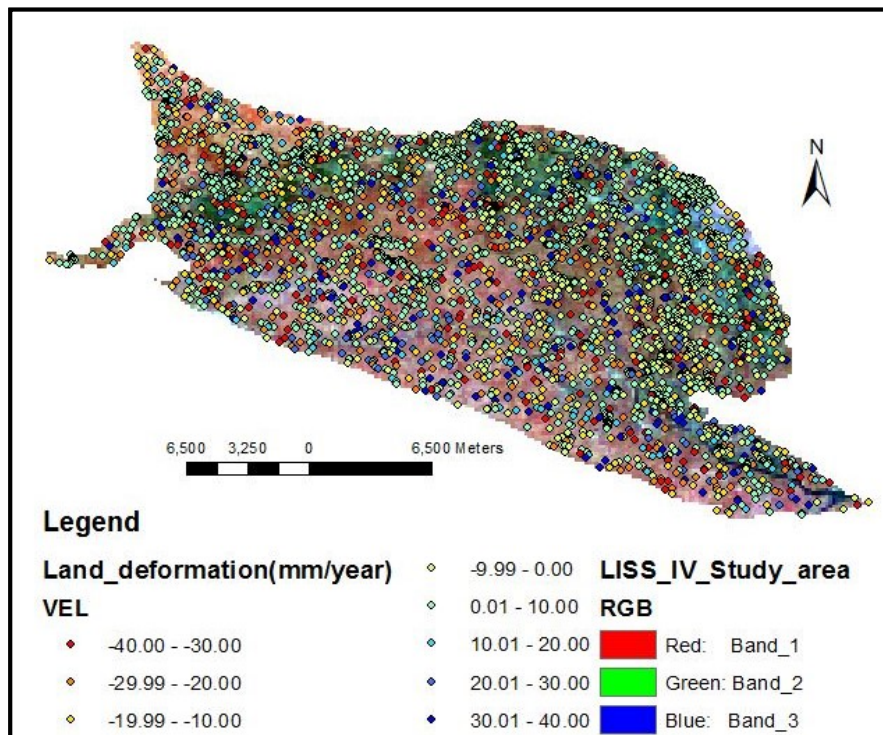
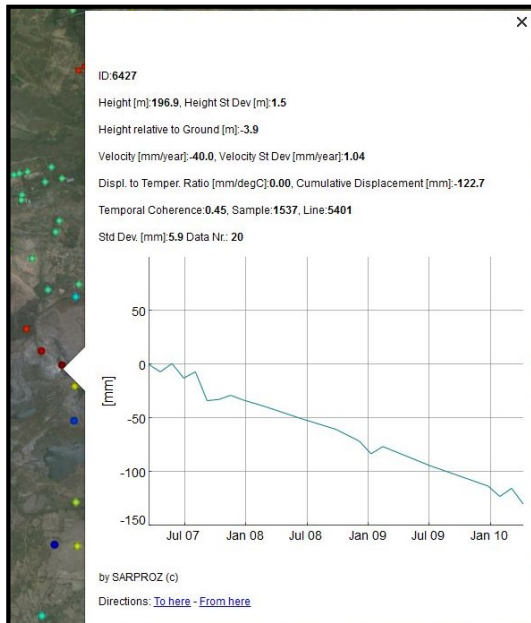
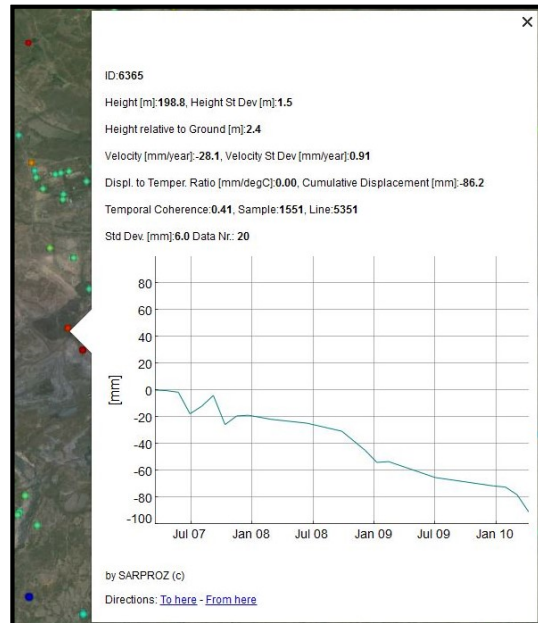


Figure 24: Land deformation information in Jharia coalfields

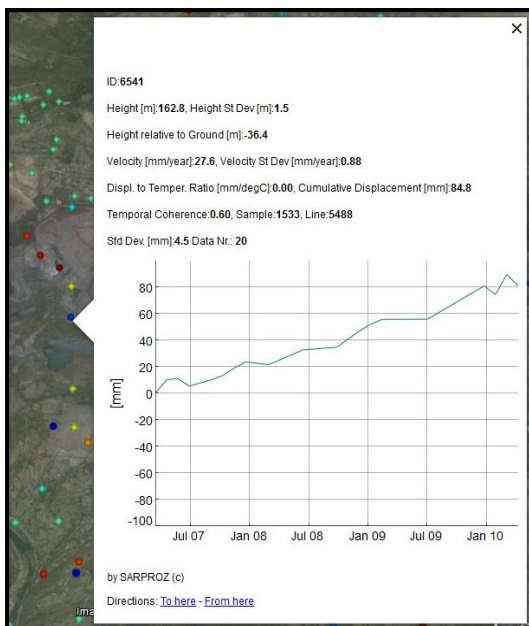
Coherence was selected 0.65 for sparse point selection and land deformation information was generated for 13068 points. The Figure 23 and Figure 24 shows the land deformation information of 3730 points within the study area. The red dot is shown in Figure 243 and Figure 244 represents the land subsidence at the rate of 40mm/year and the blue dot represents the land uplift at the rate of 40mm/year. Several red dots present adjacent to the opencast mine which represents the land deformation occurs around the opencast mines. In most of the cases, land uplift was observed near opencast mine due to the dumping of overburden. Figure 25 A-D shows the graphical representation of land deformation rate of various points such as red point, blue point, and cyan point of Figure 23.



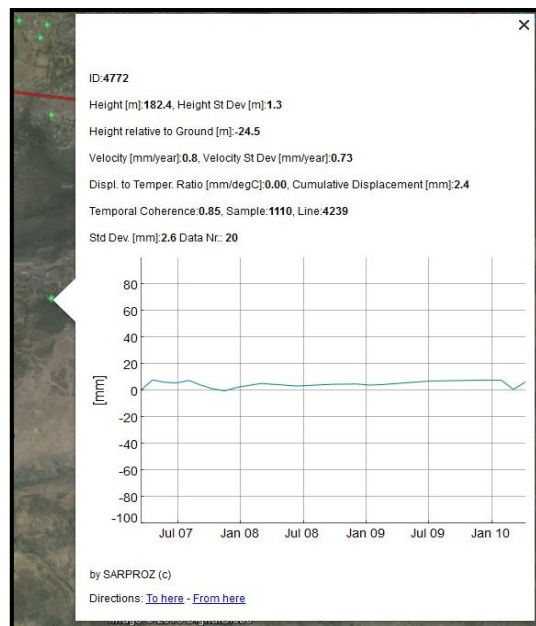
(A)



(B)



(C)



(D)

Figure 25A-D: Rate of land deformation observed at particular point over time series

Figure 25 A-B shown high rate of land subsidence i.e. 40 mm/year and 28 mm/year, respectively whereas Figure 25 C represented the high rate of land uplift i.e. 27.6 mm/year observed in opencast over burden dump area. Figure 25 D represent the point had very low deviation i.e. 0.8 mm/year of the land surface profile.

6.7. Integrated information obtain from PolSAR and ADInSAR technique

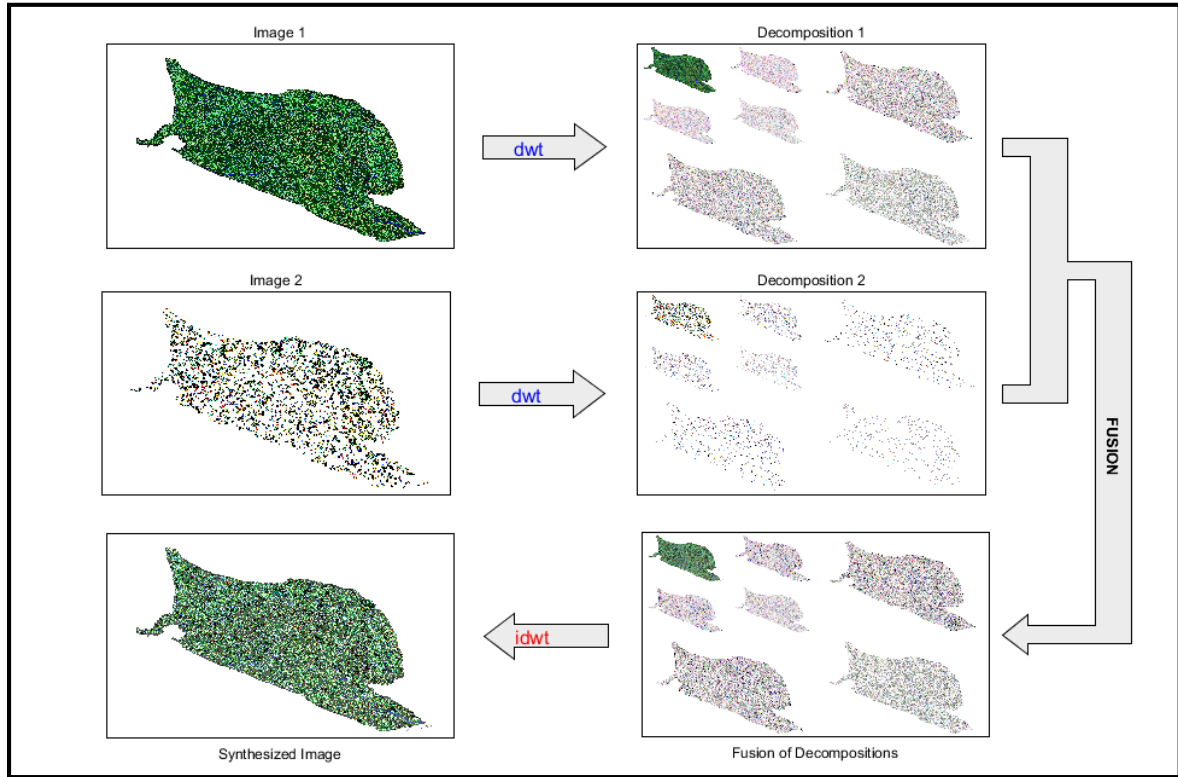


Figure 26: DWT fusion technique applied on mining properties (image 1) obtained from PolSAR data and time series land deformation information (image 2) obtained from PSInSAR technique.

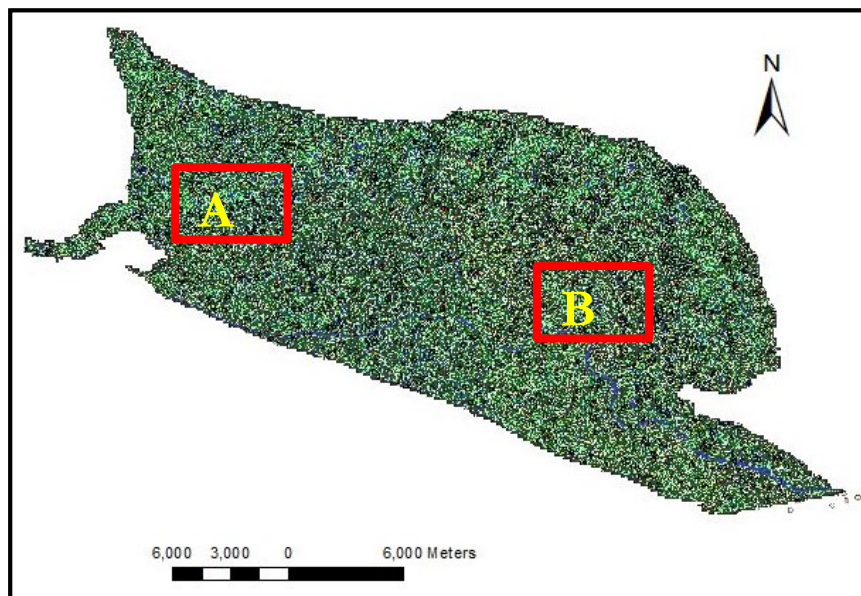
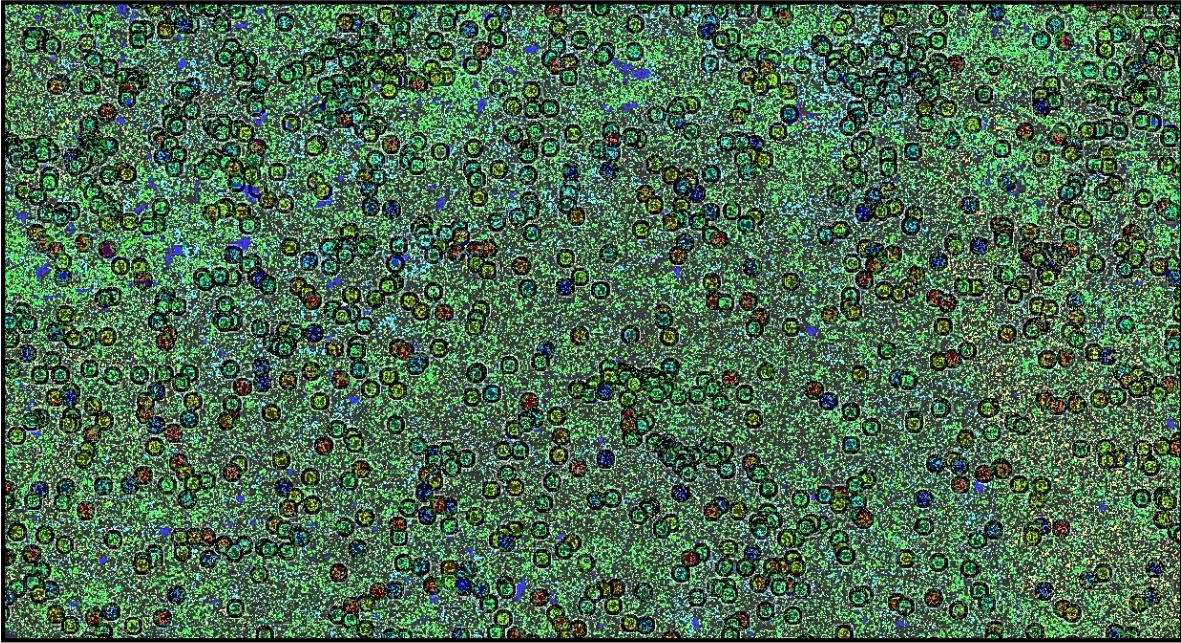


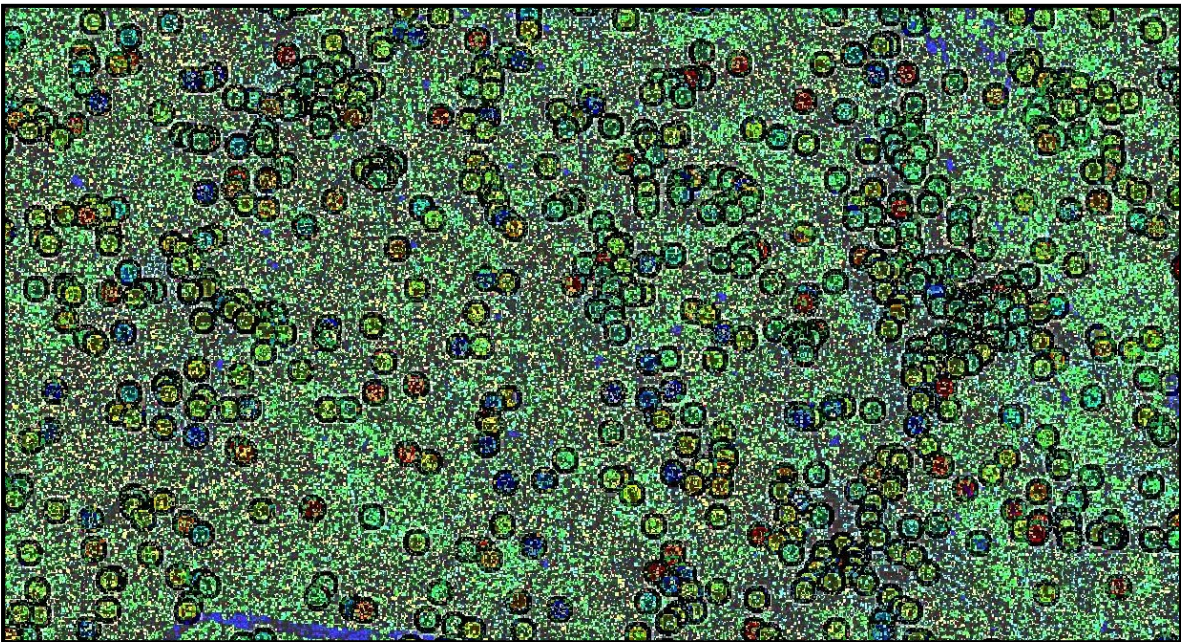
Figure 27: Fusion image of land deformation information and mining properties

Figure 26 represents a flow chart of discrete wavelet based image fusion. Two levels of decomposition were performed by using discrete wavelet transform of classified mining properties image and land deformation image corresponding to image 1 and image 2 respectively shown in Figure 26. Then fusion was performed to combine both the information in each level. Finally, inverse discrete wavelet transform was performed to generate fusion image.

Figure 27 shows fusion image of the mining properties (same as shown in Figure 17) and land deformation information (same as shown in Figure 24). Zoom area of site A and B of Figure 2627 shown below.



Zoom area "A" of Figure 27



Zoom area "B" of Figure 27

7. DISCUSSION, CONCLUSION AND RECOMMENDATIONS

7.1. Discussion

The objective of this research was the identification of opencast mining indicators and their properties; identification of land deformation in opencast mine area from single polarised SAR data and to integrate both the information. This section covers the discussion about different results achieved such as classified images of various mining properties including overall classification, consequent land deformation result obtained from time series single polarised ENVISAT data and integration of both the information including exploration of the impact of mining properties over land deformation around the opencast mine area.

The orientation angle shift varies within -23° to 23° observed from the histogram of data. Estimation of orientation angle shift in opencast mine area was observed higher compared to another area in both (2011 and 2010) polarimetric scene as shown in Figure 8 and Figure 9. Following are the impact on the elements of coherency matrix observed due to polarisation orientation angle shift.

The mean value of the T_{11} element of coherency matrix remained constant after deorientation. However, after deorientation, the mean value of the T_{22} element of coherency matrix was magnified whereas the mean value of T_{33} element of coherency matrix was reduced. The real part of the T_{23} element of coherency matrix became close to zero and the imaginary part of the T_{23} element of coherency matrix remained same. There was no consistent change observed in the real and imaginary part of the T_{12} and T_{13} element of coherency matrix. The amount of increased in double bounce power was almost similar as the amount of decreased in volume power.

Various mining properties such as HEMM and active mining faces shown in Figure 12-16, opencast mine floor mixture with soil and rock without water shown in Figure 17, opencast mine water shown in Figure 18A-B, benches and terraces shown in Figure 19, mass wasting area shown in Figure 20 were identified from fully polarimetric SAR data.

All classified HEMM points, identified on the basis of entropy value less than 0.3 and double bounce value more than 0.01, did not represent HEMMs and a large number of them (classified HEMM points) were observed in regions other than opencast mine areas, especially, came from the urban areas. Only those classified HEMM points which were found within opencast mine areas, were considered as HEMMs. Validation was performed with the five ground truth data points, as shown in Figure 13. There is the distance observed between HEMM points identified from the classified image and ground truth data. Possible reasons for the distance observed between classified HEMM points and HEMM ground truth points are as follows:

- The positions from where the ground truth data were collected may not be close to the exact locations of the HEMMs due to various reasons such as the issue of safety when the HEMMs were in operation, the factor of obtaining requisite permission and the bad condition of the improvised roads leading to the locations of HEMMs.
- A temporal difference of one month was observed between the acquisition of SAR scene and the collection of ground truth data. As the excavation work goes on continuously in the mines, the locations of HEMMs may change considerably within this period of one month.
- Another possible cause may be the movement of the equipment (HEMMs) to other excavation location, as per the decision of the mine authority.
- It may so happen that the points closer to the five ground truth data points are not highlighted in the classified image (due to the complexities in mine geometry and also because of the fact that 100% classification is very difficult to achieve).

Four out of five points were located at a distance of about 350 m from the nearest classified HEMM points was observed from Figure 13. The possible reason may be all the HEMM points were not classified by this method. Therefore, large number of ground truth data is required and with a variation of double bounce value is to be considered to explore this method to classify and validate HEMM point before say that, this method is not suitable to classify HEMM properly. However, a large number of ground truth data (greater than 30) can also be used for the preparation of training set of HEMM. Then, classification and validation of HEMM result can be performed to successful identification of HEMM. The above approach was not applied in this study to identify HEMM due to constrain of less number of ground truth data was available. Active mining faces are those where continuous excavation is going on. The excavation is done by HEMM in an opencast mine. So, the position of active mine faces in opencast mine was identified by the location of HEMM identified within the opencast area.

The successful identification of water body was done and shown in Figure 17A-B. The classified water body was validated from Google earth image. Opencast mine filled with water represents abandoned mine.

Opencast mine floor mixture with soil and rock without water was observed when mining operation such as mineral excavation, pumping was in progress. Opencast mine floor was identified in Figure 16.

Random size and shape of rocks are present in an unsystematic way in the mass wasting area. High volume scattering was observed in mass wasting area compared to single bounce and double bounce. The mass wasting area was identified and validated with Google earth image shown in Figure 19.

Overall classification was performed and shown in Figure 15. Though various polarimetric responses were come from non-mining properties, outside of the opencast mine area similar as polarimetric responses of HEMM, opencast mine floor, terrace and benches, and mass wasting area. As a result, identification of opencast mine boundary became difficult. The pure training set was prepared to minimise the effect. Shape file of each opencast mine boundary can solve this problem. Ground truth data can be used to prepare a training set to minimise the similar polarimetric responses from other than opencast mine area.

The Figure 23 and Figure 24 show the land deformation information. The red dot shown in Figure 243 and Figure 244 represents the land subsidence at the rate of 40mm/year and the blue dot represents the land uplift at the rate of 40mm/year. Graphical representations of land deformation rate of several points were shown in Figure 25 A-D. The various rate of land deformation trend of each point with respect to time series shown also in Figure 25 A-D. The land deformation trend was positive i.e. land uplift, sometimes, the land deformation rate was negative i.e. land subsidence and no land deformation was also observed for a point in various time series. Therefore, non-linear land deformation trend also monitored by using single polarised time series SAR data.

Integration of information obtained from mining properties classification and land deformation information were done by using discrete wavelet transformation operation shown in Figure 27. Several red dots were identified adjacent to the opencast mine which represents the land subsidence occurred around the opencast mines. In most of the case, land uplift observed nearby the opencast mine due to the dumping of overburden. Some of the cases land uplifts were also observed nearby the dumping area. The high rate of land deviation (subsidence or uplift) was observed around the opencast mine and the effect of land deformation due to opencast mining activities was lesser as one goes away from the opencast mine, shown in the zoom area A-B of Figure 27.

7.2. Conclusion

Recently, few researchers are interested in monitoring opencast mine activities by using SAR. However, SAR technology is not explored in various opencast mine related problems till now. Identification and monitoring of various opencast mining activities including hazards monitoring become necessary to explore the capabilities of SAR technology.

After orientation angle compensation, the volume power is reduced and the double bounce power is magnified. The amount of rise in double bounce power is almost similar as the amount of reduction in volume power.

Identification of various opencast mining indicators and their properties are easy to classify. However, similar polarimetric responses are observed from benches and terraces of opencast mine and opencast mine floor as urban areas and barren lands, respectively. Therefore, identification of opencast mine boundary becomes difficult from the classified image. Identification of various opencast mining indicators and their properties become more difficult when opencast mine area is closely surrounded by slum area. The HEMM ground truth points and classified HEMM points located 350 m (approximate) apart was observed from Figure 13. The possible reason may be all the HEMM were not classified by this method. However, due to the unavailability of the adequate ground truth data validation could not be done very efficiently in this study. A large number of ground truth data points, should be required at exact locations of the HEMMs within a very short time interval after the acquisition of the SAR data, is needed for both classification (i.e., the preparation of the training set) and validation. Anyway, the application of SAR for classification of mining indicators and their properties in opencast mines, is a new field where most probably no work has been done previously. And I hope that, in future, the method adopted in this study will be employed efficiently (with adequate data) to generate useful and interesting results.

Implementation of SAR technology for land deformation is also very challenging because of various opencast mine's slope angle and direction and its dynamic nature. It is observed that 37.23% of 3730 points shows more than ± 10 mm/year land deformation rate in this study area. Maximum number of land deformation points (deformation rate more than ± 10 mm/year) are located adjoining the opencast mining areas. The high rate of land deviation (subsidence or uplift) observed nearer the opencast mine area and the effect of land deformation due to opencast mining activities was lesser as one goes away from the opencast mine. The spatial relationship between land deformation and mining indicators and their properties was also observed from discrete wavelet based fused image. So, the spatial relation between land deformation and mining indicators and their properties responsible for land deformation cannot be denied.

7.3. Answer to the research questions

- 1) What is the influence of polarisation orientation angle on PolSAR data of opencast mine topography?

The estimated value of the shift in orientation angle was observed to be higher in opencast mine areas than in other areas in the fully polarimetric scenes corresponding to both 2011 and 2010 as shown in Figures 8 and 9 respectively.

- 2) Which of the polarimetric signatures and decomposition methods are best suited for identification of mining indicators and their properties responsible for opencast mine induced land deformation?

HEMM contributed high double bounce value and low entropy value ($H < 0.3$) and opencast active mine faces were identified from the location of HEMM.

The opencast water body was identified by high single bounce value and high entropy value.

Opencast mine floor without water was generated by the polarimetric responses of medium single bounce and medium entropy value.

Benches and terraces were identified by higher double bounce scattering compared to other mining properties except for HEMM.

The mass wasting areas were identified by higher volume scattering compared to other mining properties.

- 3) What are the spatial patterns and position of land deformation identified by time series analysis of

PSInSAR process?

The high rate of land deformation is observed mainly around the opencast mine area and the effect of land deformation due to opencast mining activities is lesser as one goes away from the opencast mine.

- 4) Is DInSAR fail in specific mine area?? In which state DInSAR process failed and which respective characteristic or property of opencast mine is responsible for the failure?

Failure of DInSAR did not observe in this study. Possible causes for DInSAR failure are described in the motivation and problem statement section.

- 5) How to integrate the PolSAR and PSInSAR results?

Integration of the retrieved information from the PolSAR and PSInSAR results were done by the discrete wavelet fusion operation. However, discrete wavelet fusion operation preserves both spatial and spectral information from both the images, still, detail information extraction from fused image was not so successful due to non-differentiate of opencast mining area from its surroundings. Therefore, shape file of each opencast mine boundary can be a solution to understand the land deformation trend with respect to mining properties.

7.4. Recommendation

Large number (> 50 for each class) of ground truth data is required for creating training set and validation of results. Accurate and precise ground truth data should be collected. Accuracy assessment of classification results is necessary to justify the classification of mining properties. Sequential time series single polarised SAR image scenes are required for continuous monitoring of land deformation. Best decomposition method can be identified by comparison of accuracy result of various classified mining properties in various decomposition methods.

C-band is less sensitive to polarisation orientation angle shift compare to P-band and L-band. Effect of polarisation orientation angle shift on opencast mine topography can also be studied by using P-band and L-band.

LIST OF REFERENCES

- Altun, A. O., Yilmaz, I., & Yildirim, M. (2010). A short review on the surficial impacts of underground mining. *Scientific Research and Essays*, 5(21), 3206 – 3212. <https://doi.org/10.5897/SRE>
- Bell, F. G., Stacey, T. R., & Genske, D. D. (2000). Mining subsidence and its effect on the environment: some differing examples. *Environmental Geology*, 40(1-2), 135–152. <https://doi.org/10.1007/s002540000140>
- Bitelli, G., Bonsignore, F., Conte, S. Del, Novali, F., Pellegrino, I., & Vittuari, L. (2015). Integrated Use of Advanced InSAR and GPS Data for Subsidence Monitoring. In *Engineering Geology for Society and Territory* (Vol. 5, pp. 147–150). Cham: Springer International Publishing. https://doi.org/10.1007/978-3-319-09048-1_29
- Chatterjee, R. S., Thapa, S., Singh, K. B., Varunakumar, G., & Raju, E. V. R. (2015). Detecting, mapping and monitoring of land subsidence in Jharia Coalfield, Jharkhand, India by spaceborne differential interferometric SAR, GPS and precision levelling techniques. *Earth System Science*, 124(6), 1359–1376.
- Cloude, S. R. (2009). Polarized point scatterers: An algorithm for detection using ALOS-PALSAR data. In *International Geoscience and Remote Sensing Symposium (IGARSS)* (Vol. 5, pp. 150–153). <https://doi.org/10.1109/IGARSS.2009.5417709>
- Colombo, D., & Tre, T. E. (2013). Measuring deformation from space. InSAR as an operational tool for mining sector. In *South African Smart Grid Initiative (SASGI)* (pp. 1 – 9). Retrieved from <http://www.ee.co.za/wp-content/uploads/2014/05/Davide-Colombo.pdf>
- Crosetto, M. (2002). Calibration and validation of SAR interferometry for DEM generation. *ISPRS Journal of Photogrammetry and Remote Sensing*, 57(3), 213–227. [https://doi.org/10.1016/S0924-2716\(02\)00107-7](https://doi.org/10.1016/S0924-2716(02)00107-7)
- Dhillon, B. S., & Anude, O. C. (1992). Mining equipment reliability: A review. *Microelectronics Reliability*, 32(8), 1137 – 1156. Retrieved from <http://www.sciencedirect.com/science/article/pii/002627149290033H>
- Dong, J., Zhuang, D., Huang, Y., & Fu, J. (2009). Advances in multi-sensor data fusion: Algorithms and applications. *Sensors*, 9(10), 7771–7784. <https://doi.org/10.3390/s9100771>
- Erban, L. E., Gorelick, S. M., & Zebker, H. A. (2014). Groundwater extraction, land subsidence, and sea-level rise in the Mekong Delta, Vietnam. *Environmental Research Letters*, 9(8), 084010. <https://doi.org/10.1088/1748-9326/9/8/084010>
- Esmailzade, M., Amini, J., & Zakeri, S. (2015). Georeferencing on Synthetic Aperture RADAR imagery. In *International Conference on Sensors & Models in Remote Sensing & Photogrammetry* (pp. 179 – 184). Kish Island, Iran: Photogrammetry, Remote Sensing and Spatial Information Sciences. <https://doi.org/10.5194/isprsarchives-XL-1-W5-179-2015>
- Ferretti, A., Guarnieri, A. M., Prati, C., & Rocca, F. (2007a). *InSAR Principles: Guidelines for SAR Interferometry Processing and Interpretation*. (K. Fletcher, Ed.). Noordwijk, The Netherlands: European Space Agency. Retrieved from http://www.esa.int/esapub/tm/tm19/TM-19_ptA.pdf
- Ferretti, A., Guarnieri, A. M., Prati, C., & Rocca, F. (2007b). InSAR processing: a practical approach. In K. Fletcher (Ed.) (p. 71).

- Freeman, A., & Durden, S. L. (1998). A three-component scattering model for polarimetric SAR data. *IEEE Transactions on Geoscience and Remote Sensing*, 36(3), 963–973. <https://doi.org/10.1109/36.673687>
- Gao, L., & Ban, Y. (2008). Investigating the performance of SAR polarimetric features in land-cover classification. *The International Archives of the Photogrammetry, Remote Sensing and Spatial Information Sciences*, XXXVII Par(1), 317 – 322.
- Geomartin. (2009). Twin creeks gold mine, Nevada, USA. Retrieved September 11, 2016, from <https://en.wikipedia.org/wiki/File:Twincreeksblast.jpg>
- Ghose, M. K. (2007). Opencast coal mining in India: Analyzing and addressing the air environmental impacts. *Environmental Quality Management*, 16(3), 71–87. <https://doi.org/10.1002/tqem.20132>
- Gupta, M., Mohanty, K. K., Kumar, D., & Banerjee, R. (2014). Monitoring surface elevation changes in Jharia coalfield, India using synthetic aperture radar interferometry. *Environmental Earth Sciences*, 71(6), 2875–2883. <https://doi.org/10.1007/s12665-013-2664-9>
- Hartman, H. L., & Mutmanský, J. M. (2002). *Introductory mining engineering*. Wiley-India (second). John Wiley & Sons. Retrieved from <http://books.google.com/books?hl=en&lr=&id=jPdF6K0at4YC&oi=fnd&pg=PR11&dq=Introductory+Mining+Engineering&ots=AFva5Ucl4N&sig=RQxRzSBefZqw5T8f11z1n24wEic>
- Hartwig, M. E., Paradella, W. R., & Mura, J. C. (2013). Detection and monitoring of surface motions in active open pit iron mine in the amazon region, using persistent scatterer interferometry with terraSAR-X satellite data. *Remote Sensing*, 5(9), 4719–4734. <https://doi.org/10.3390/rs5094719>
- Heavy Equipment. (2016). EARTHMOVING & MINING. Retrieved August 26, 2016, from <http://www.heavyequipment.com/heavy-equipment/earthmoving-mining>
- Herrera, G., Tomás, R., Vicente, F., Lopez-Sanchez, J. M., Mallorquí, J. J., & Mulas, J. (2010). Mapping ground movements in open pit mining areas using differential SAR interferometry. *International Journal of Rock Mechanics and Mining Sciences*, 47(7), 1114–1125. <https://doi.org/10.1016/j.ijrmms.2010.07.006>
- Hong, S., Moon, W. M., Paik, H.-Y., & Choi, G.-H. (2002). Data Fusion of multiple Polarimetric SAR images using Discrete Wavelet Transform (DWT). *IEEE*, 3323–3325.
- Hu, J., Li, Z. W., Ding, X. L., Zhu, J. J., Zhang, L., & Sun, Q. (2014). Resolving three-dimensional surface displacements from InSAR measurements: A review. *Earth-Science Reviews*, 133, 1–17. <https://doi.org/10.1016/j.earscirev.2014.02.005>
- Hustrulid, W. A., & Clark, G. B. (2016). Mining. Retrieved June 1, 2016, from <http://www.britannica.com/technology/mining>
- Iannacone, J. P., & Falorni, G. (2016). Towards InSAR guidelines for landslide monitoring Towards InSAR guidelines for landslide monitoring. Retrieved from https://www.researchgate.net/profile/Jean_Pascal_Iannacone/publication/309593043_Towards_InSAR_guidelines_for_landslide_monitoring/links/5819117708ae6378919e8259.pdf

- Jakóbczyk, J., Cala, M., & Stopkowicz, A. (2015). What Were the Reasons for the Rapid Landslide Occurrence in “Piaseczno” Open Pit? – Analysis of the Landslide Process. *Studia Geotechnica et Mechanica*, 37(1). <https://doi.org/10.1515/sgem-2015-0004>
- Jarosz, A., & Wanke, D. (2004). Use of InSAR for monitoring of mining deformations. *European Space Agency, (Special Publication) ESA SP*, (550), 283–288. Retrieved from http://earth.esa.int/workshops/fringe03/proceedings/posters/51_jarosz.pdf
- Jayanthu, S., & Reddy, C. V. (2008). *Design of optimum slopes for safety and conservation in opencast mines – an appraisal*. Retrieved from <http://dspace.nitrkl.ac.in/dspace/bitstream/2080/1704/1/PAPER5-slope-stabilit-RAIPUR-MINTECH11-Prof Jayanth-Mr VReddy.pdf>
- Kajimoto, M., & Susaki, J. (2013). Urban-area extraction from polarimetric SAR images using polarization orientation angle. *IEEE Geoscience and Remote Sensing Letters*, 10(2), 337–341. <https://doi.org/10.1109/LGRS.2012.2207085>
- Kulshreshtha, M., & Parikh, J. K. (2002). Study of efficiency and productivity growth in opencast and underground coal mining in India: a DEA analysis. *Energy Economics*, 24(5), 439–453. [https://doi.org/10.1016/S0140-9883\(02\)00025-7](https://doi.org/10.1016/S0140-9883(02)00025-7)
- Lakshmi, S. S., Patra, S. K., Saibaba, J., & Varadan, G. (2012). Polarimetric SAR data analysis for identification and characterisation of ships - Geospatial World. Retrieved August 16, 2016, from <http://www.geospatialworld.net/article/polarimetric-sar-data-analysis-for-identification-and-characterisation-of-ships/>
- Lee, J. S., Ainsworth, T. L., Schuler, D. L., Kasilingam, D., & Boerner, W. M. (2001). Interpreting off-diagonal terms in polarimetric coherency matrix. *International Geoscience and Remote Sensing Symposium (IGARSS)*, 2(202), 913–915. <https://doi.org/10.1109/IGARSS.2001.976678>
- Lee, J. S., & Schuler, D. (2003). Polarization orientation estimation and applications: a review. *Igarss*, 00(C), 428–430. <https://doi.org/10.1109/IGARSS.2003.1293798>
- Lee, J. Sen, & Ainsworth, T. L. (2011). The effect of orientation angle compensation on coherency matrix and polarimetric target decompositions. In *IEEE Transactions on Geoscience and Remote Sensing* (Vol. 49, pp. 53–64). <https://doi.org/10.1109/TGRS.2010.2048333>
- Lee, J. Sen, & Pottier, E. (2009). *Polarimetric radar imaging: From basics to applications*. (B. J. Thompson, Ed.). Boca Raton: CRC Press. Retrieved from [http://ezproxy.utwente.nl:2201/\(S\(ua1kldkunbjfdvmffobjvuil\)\)/Reader.aspx?p=427062&o=1200&u=Gp3B6htiKSD0GgJUf3t4nQ==&t=1463999605&h=E008A6271F06502F125284487105C8A0A84B6063&s=45406017&ut=3997&pg=1&r=img&c=-1&pat=n&cms=-1&sd=2](http://ezproxy.utwente.nl:2201/(S(ua1kldkunbjfdvmffobjvuil))/Reader.aspx?p=427062&o=1200&u=Gp3B6htiKSD0GgJUf3t4nQ==&t=1463999605&h=E008A6271F06502F125284487105C8A0A84B6063&s=45406017&ut=3997&pg=1&r=img&c=-1&pat=n&cms=-1&sd=2)
- Lee, J. Sen, Schuler, D. L., & Ainsworth, T. L. (2000). Polarimetric SAR data compensation for terrain azimuth slope variation. *IEEE Transactions on Geoscience and Remote Sensing*, 38(5 I), 2153–2163. <https://doi.org/10.1109/36.868874>
- Lee, J. Sen, Schuler, D. L., Ainsworth, T. L., Krogager, E., Kasilingam, D., & Boerner, W. M. (2002). On the estimation of radar polarization orientation shifts induced by terrain slopes. *IEEE Transactions on Geoscience and Remote Sensing*, 40(1), 30–41. <https://doi.org/10.1109/36.981347>
- Loupasakis, C., Angelitsa, V., Rozos, D., & Spanou, N. (2014). Mining geohazards—land subsidence caused by the dewatering of opencast coal mines: The case study of the Amyntaio coal mine, Florina, Greece. *Natural Hazards*, 70(1), 675–691. <https://doi.org/10.1007/s11069-013-0837-1>

- Lu, Z., Jung, H.-S., Zhang, L., Lee, W., Lee, C.-W., & Dzurisin, D. (2013). Digital elevation model generation from satellite interferometric synthetic aperture radar. In X. Yang & J. Li (Eds.), *Advances in Mapping from Remote Sensor Imagery: Techniques and Applications* (pp. 119 – 144). CRC Press: Taylor & Francis Group.
- Meisina, C., Zucca, F., Fossati, D., Ceriani, M., & Allievi, J. (2006). Ground deformation monitoring by using the Permanent Scatterers Technique: The example of the Oltrepo Pavese (Lombardia, Italy). *Engineering Geology*, 88(3-4), 240–259. <https://doi.org/10.1016/j.enggeo.2006.09.010>
- Milczarek, W., Blachowski, J., & Grzempowski, P. (2017). Application of PSInSAR for assessment of surface deformations in post_mining area _ case study of the former Walbrzych Hard Coal Basin (SW Poland). *Acta Geodynamica et Geomaterialia*, 14(1(185)), 41–52. <https://doi.org/10.13168/AGG.2016.0026>
- Mura, J. C., Paradella, W. R., Gama, F. F., Santos, A. R., Galo, M., Camargo, P. O., ... Silva, G. G. (2014). Monitoring of surface deformation in open pit mine using DInSAR time-series: a case study in the N5W iron mine (Carajás, Brazil) using TerraSAR-X data. In C. Notarnicola, S. Paloscia, & N. Pierdicca (Eds.), *Society of Photographic Instrumentation Engineers* (Vol. 9243, p. 924311). <https://doi.org/10.1117/12.2066886>
- Mura, J. C., Paradella, W. R., Gama, F. F., Silva, G. G., Galo, M., Camargo, P. O., ... Silva, A. (2016). Monitoring of Non-Linear Ground Movement in an Open Pit Iron Mine Based on an Integration of Advanced DInSAR Techniques Using TerraSAR-X Data. *Remote Sensing*, 8(5), 409. <https://doi.org/10.3390/rs8050409>
- Natural Resource Canada. (2014). Radar Polarimetry. Retrieved November 4, 2016, from <http://www.nrcan.gc.ca/earth-sciences/geomatics/satellite-imagery-air-photos/satellite-imagery-products/educational-resources/9275>
- Ng, A. H.-M., Chang, H.-C., Ge, L., Rizos, C., & Omura, M. (2009). Assessment of radar interferometry performance for ground subsidence monitoring due to underground mining. *Earth Planets Space*, 61, 733–745.
- Nunziata, F., Migliaccio, M., & Brown, C. E. (2012). Reflection symmetry for polarimetric observation of man-made metallic targets at sea. *IEEE Journal of Oceanic Engineering*, 37(3), 384–394. <https://doi.org/10.1109/JOE.2012.2198931>
- Ogden, R. T. (1997). *Essential Wavelets for Statistical Applications and Data Analysis* (1st ed.). New York: Springer Science + Business Media. <https://doi.org/10.1007/978-1-4612-0709-2>
- Osasan, K. S., & Afeni, T. B. (2010). Review of surface mine slope monitoring techniques. *Journal of Mining Science*, 46(2), 177 – 186. Retrieved from <http://link.springer.com/article/10.1007/s10913-010-0023-8>
- Pankow, K. L., Moore, J. R., Hale, J. M., Koper, K. D., Kubacki, T., Whidden, K. M., & McCarter, M. K. (2014). Massive landslide at Utah copper mine generates wealth of geophysical data. *GSA Today*, 4–9. <https://doi.org/10.1130/GSATG191A.1>
- Paradella, W. R., Ferretti, A., Mura, J. C., Colombo, D., Gama, F. F., Tamburini, A., ... Gomes, L. L. (2015). Mapping surface deformation in open pit iron mines of Carajás Province (Amazon Region) using an integrated SAR analysis. *Engineering Geology*, 193, 61–78. <https://doi.org/10.1016/j.enggeo.2015.04.015>

- Paradella, W. R., Mura, J. C., Gama, F. F., Santos, A. R., Silva, G. G., Galo, M., ... Silva, A. Q. (2015). Complementary Use of Information From Space-Based Dinsar and Field Measuring Systems for Operational Monitoring Purposes in Open Pit Iron Mines of Carajás Mining Complex (Brazilian Amazon Region). *ISPRS - International Archives of the Photogrammetry, Remote Sensing and Spatial Information Sciences*, XL-7/W3(May), 905–911. <https://doi.org/10.5194/isprsarchives-XL-7-W3-905-2015>
- Pinto, C. d. A., Paradella, W. R., Mura, J. C., Gama, F. F., dos Santos, A. R., & Silva, G. G. (2014). Results of the application of persistent scatterers interferometry for surface displacements monitoring in the Azul open pit manganese mine (Carajás Province, Amazon region) using TerraSAR-X data. In U. Michel & K. Schulz (Eds.) (Vol. 9245, p. 92451K). <https://doi.org/10.1117/12.2067233>
- Pinto, C. de A., Paradella, W. R., Mura, J. C., Gama, F. F., Santos, A. R. dos, Silva, G. G., & Hartwig, M. E. (2015). Applying persistent scatterer interferometry for surface displacement mapping in the Azul open pit manganese mine (Amazon region) with TerraSAR-X StripMap data. *Journal of Applied Remote Sensing*, 9(1), 095978 1 – 18. <https://doi.org/10.1117/1.JRS.9.095978>
- Pohl, C., Munro, D., & Genderen, J. L. van. (1997). Enhanced image analysis through multilevel data fusion techniques. In *SPIE - The International Society for Optical Engineering* (Vol. 3068, pp. 32–39). <https://doi.org/10.1117/12.280821>
- Pohl, C., & van Genderen, J. (2015). Structuring contemporary remote sensing image fusion. *International Journal of Image and Data Fusion*, 6(1), 3–21. <https://doi.org/10.1080/19479832.2014.998727>
- Prakash, A., & Gupta, R. P. (1998). Land-use mapping and change detection in a coal mining area - a case study in the Jharia coalfield, India. *International Journal of Remote Sensing*, 19(3), 391–410.
- R Core Team (2015). R: A language and environment for statistical computing. R Foundation for Statistical Computing, Vienna, Austria. URL <http://www.R-project.org/>.
- Raspini, F., Bianchini, S., Moretti, S., Loupasakis, C., Rozos, D., Duro, J., & Garcia, M. (2016). Advanced interpretation of interferometric SAR data to detect, monitor and model ground subsidence: outcomes from the ESA-GMES TerraFirma project. *Natural Hazards*, 1–27. <https://doi.org/10.1007/s11069-016-2341-x>
- Rosen, P. A., Hensley, S., Joughin, I. R., Li, F. K., Madsen, S. N., Rodríguez, E., & Goldstein, R. M. (2000). Synthetic Aperture Radar Interferometry. In *PROCEEDING OF THE IEEE* (Vol. 88, pp. 333– 382). Retrieved from http://www.grapenthin.org/teaching/geop572_2015/download/Rosen_etal_2000_InSAR.pdf
- Savage, C. N. (1951). Mass-Wasting, Classification and Damage in OHIO. *The Ohio Journal of Science*, 51(6), 299 – 308. Retrieved from <http://hdl.handle.net/1811/3871>
- Schneider, R. Z., Papathanassiou, K. P., Hajnsek, I., & Moreira, A. (2006). Polarimetric and interferometric characterization of coherent scatterers in urban areas. In *IEEE Transactions on Geoscience and Remote Sensing* (Vol. 44, pp. 971–983). <https://doi.org/10.1109/TGRS.2005.860950>
- Simone, G., Farina, A., Morabito, F. C., Serpico, S. B., & Bruzzone, L. (2002). *Image fusion techniques for remote sensing application. Department of Information and Communication technology* (Vol. 3).
- Simone, G., Morabito, F. C., & Farina, A. (2001). Multifrequency and Multiresolution Fusion of SAR Images for Remote Sensing Applications. In *International Conference on Information Fusion* (pp. 1 – 8). Montreal, Canada.

- Singh, G., Yamaguchi, Y., & Park, S. (2013). General Four-Component Scattering Power Decomposition With Unitary Transformation of Coherency Matrix, *51*(5), 3014–3022.
- Sousa, J. J., Ruiz, A. M., Hanssen, R. F., Bastos, L., Gil, A. J., Galindo-Zaldívar, J., & Sanz de Galdeano, C. (2010). PS-InSAR processing methodologies in the detection of field surface deformation-Study of the Granada basin (Central Betic Cordilleras, southern Spain). *Journal of Geodynamics*, *49*(3-4), 181–189. <https://doi.org/10.1016/j.jog.2009.12.002>
- Strzelczyk, J., & Porzycka-Strzelczyk, S. (2014). Identification of coherent scatterers in SAR images based on the analysis of polarimetric signatures. *IEEE Geoscience and Remote Sensing Letters*, *11*(4), 783–787. <https://doi.org/10.1109/LGRS.2013.2279005>
- Turkar, V., & Rao, Y. S. (2011). Effect of Different Target Decomposition Techniques on Classification Accuracy for Polarimetric SAR Data. *Communications in Computer and Information Science*, *145*, 138–145.
- Verma, R. (2012). *Polarimetric decomposition based on general characterisation of scattering from urban areas and multiple component scattering model*. University of Twente. Retrieved from http://www.iirs.gov.in/iirs/sites/default/files/StudentThesis/Verma_Ruchi_28154_Thesis.pdf
- Wang, S. (1981). On the mechanism and process of slope deformation in an open pit mine. *Rock Mechanics Felsmechanik Mecanique Des Roches*, *13*(3), 145–156. <https://doi.org/10.1007/BF01239035>
- Yamaguchi, Y., Moriyama, T., Ishido, M., & Yamada, H. (2005). Four-component scattering model for polarimetric SAR image decomposition. *IEEE Transactions on Geoscience and Remote Sensing*, *43*(8), 1699–1706. <https://doi.org/10.1109/TGRS.2005.852084>
- Yamaguchi, Y., Sato, A., Boerner, W. M., Sato, R., & Yamada, H. (2010). Four-component scattering power decomposition with rotation of coherency matrix. In *International Geoscience and Remote Sensing Symposium (IGARSS)*. <https://doi.org/10.1109/IGARSS.2010.5650768>
- Yang, H., Peng, J., & Ding-xuant, Z. (2012). *Slope of Large-scale Open-pit Mine Monitoring Deformations by Using Ground-Based Interferometry*. Retrieved from <http://dma.lsgi.polyu.edu.hk/JISDM-Proceeding/Proceeding/Full paper/168.pdf>
- Zhang, L., Zou, B., Cai, H., & Zhang, Y. (2008). Multiple-component scattering model for polarimetric SAR image decomposition. *IEEE Transactions on Geoscience and Remote Sensing*, *5*(4), 603–607. <https://doi.org/10.1109/LGRS.2008.2000795>